International Journal of Impact Engineering 148 (2021) 103767

Contents lists available at ScienceDirect

International Journal of Impact Engineering

journal homepage: www.elsevier.com/locate/ijimpeng

Dynamic impact testing of cellular solids and lattice structures: Application of two-sided direct impact Hopkinson bar

Tomáš Fíla [*,a], Petr Koudelka [a], Jan Falta [a], Petr Zlámal [a], Václav Rada [a,b], Marcel Adorna [a], Stefan Bronder [c], Ondřej Jiroušek [a]

[a] Czech Technical University in Prague, Faculty of Transportation Sciences, Konviktská 20, Prague 110 00, Czech Republic
[b] Czech Academy of Sciences, Institute of Theoretical and Applied Mechanics, Prosecká 809/76, Prague 190 00, Czech Republic
[c] Saarland University, Applied Mechanics, Campus A4.2, Saarbruecken 661 23, Germany

ARTICLE INFO

Keywords:
Direct impact Hopkinson bar
Cellular solids
Auxetic metamaterials
Digital image correlation
Wave separation

ABSTRACT

Direct impact testing with a Hopkinson bar is, nowadays, a very popular experimental technique for investigating the behavior of cellular materials, e.g., lattice metamaterials, at high strain-rates as it overcomes several limitations of the conventional Split Hopkinson Pressure Bar (SHPB). However, standard direct impact Hopkinson bars (DIHB) have only single-sided instrumentation complicating the analysis. In this paper, a DIHB apparatus instrumented with conventional strain-gauges on both bars (a so called Open Hopkinson Pressure Bar - OHPB) is used for dynamic impact experiments of cellular materials. Digital image correlation (DIC) is used as a tool for investigating the displacements and velocities at the faces of the bars. A straight-forward wave separation technique combining the data from the strain-gauges with the DIC is adopted to increase the experiment time window multiple times. The experimental method is successfully tested at impact velocities in a range of 5 – 30 $m \cdot s^{-1}$ with both linear elastic and visco-elastic bars of a medium diameter. It is shown that, under certain circumstances, a simple linear elastic model is sufficient for the evaluation of the measurements with the visco-elastic bars, while no additional attenuation and phase-shift corrections are necessary. The applicability of the experimental method is demonstrated on various experiments with conventional metal foams, hybrid foams, and additively manufactured auxetic lattices subjected to dynamic compression.

1. Introduction

The dynamic testing of materials is an important task for describing the deformation behavior at high strain-rates and for understanding phenomena like wave propagation, inertia and friction effects, shock front formation, or coupled thermo-mechanical effects [1]. For such high strain-rate testing, Hopkinson bar experimental techniques have been found to be a vital method that produces reliable and consistent results. Nowadays, extensive research is performed in the field of cellular solids like metal foams [2,3], hybrid foams [4], additively manufactured materials [5], or lattice structures and metamaterials [6] including materials with a negative Poisson's ratio (auxetics) [7–12]. In this field, the behavior of cellular solids and metamaterials can be used for the development of, e.g., lightweight structures of complex shapes or shock absorbers [13]. However, as the internal structure of cellular solids and metamaterials is rather complex (often on all levels: micro, mezzo or macro), the description of their mechanical properties is non-trivial, dependent on many factors, and their behavior often exhibits mechanisms that are still not well described and understood. This problem is particularly significant in dynamic loading, where a lot of effects influence the deformation behavior of the material. While the standard Kolsky bar arrangement [14] is a well-established technique for the high strain-rate testing of bulk materials in compression, it has a number of disadvantages limiting its application for cellular solids and additively manufactured lattices [15,16]. Nevertheless, the topic is very attractive and papers describing the experimental and/or numerical investigation of metal foams [17–21], metamaterials or additively manufactured materials and lattices [22] using the Hopkinson bar or gas-/powder-gun [23,24] are available. In some papers, digital image correlation (DIC) has been employed as a tool for the advanced analysis of the displacement and strain fields during the experiments [25–28]. The dynamic indentation of cellular materials subjected to dynamic loading has also been of interest [29–34].

In the conventional split Hopkinson pressure bar (SHPB), the

* Corresponding author.
E-mail addresses: fila@fd.cvut.cz, filatoma@fd.cvut.cz (T. Fíla).

https://doi.org/10.1016/j.ijimpeng.2020.103767
Received 20 May 2020; Received in revised form 14 September 2020; Accepted 1 November 2020
Available online 5 November 2020

maximum achievable strain in the specimen is proportional to the length of the striker bar and its impact velocity. Therefore, the maximum strain is significantly constrained by the geometry of the setup and performance of its mechanism accelerating the striker. Moreover, in classical theory, the time window of the experiment is limited to the short period of time before the wave superposition occurs at the location of the strain wave sensing instrument (typically a strain-gauge). As the cellular solids and lattices are materials with a relatively low mechanical impedance, another problem arises with the disproportion between the amplitudes of the reflected and transmitted signal that are additionally distorted by the wave dispersion. Typically, the transmitted signal is much lower in comparison with the amplitude of the incident and reflected pulse making the analysis of dynamic equilibrium difficult. Due to the complex nature of cellular solids and lattices, another problem is related to the specimen size. The testing of the representative volume element (RVE), as defined for cellular solids [35], usually requires large specimens that can barely be tested up to the densification region in the classical Kolsky bar. Here, larger strain of the specimen can be achieved by increase of the striker bar impact velocity or by increase of striker bar length. Both approaches have their physical limits. The maximum striker bar impact velocity in the SHPB is limited by the performance of the device for the acceleration of the striker (typically a gas-gun) and by the yield strength of the material of the bars. As the incident pulse is generated by the impact of the striker on the incident bar, the amplitude of the pulse is much higher than the pulse transmitted through the specimen. Therefore, an apparent velocity limit exists that would result in the plastic deformation of the bar (e.g., for aluminum alloys approximately $50-60\,\mathrm{m{\cdot}s^{-1}}$). On the other hand, an increase in the striker bar length is limited by the geometrical tolerances of the gas-gun barrel. Generally, longer strikers have to be used for testing at lower strain-rates to achieve a similar strain as those by shorter strikers at higher velocities. Moreover, large specimens require a long time to achieve an equilibrium of the dynamic forces.

Many improvements in the standard Hopkinson bar experimental setup have been developed to overcome the aforementioned problems, to extend its application envelope and to reliably test cellular solids and low impedance materials in general. Pulse-shaping techniques [36–41] have been used to reduce the wave dispersion in the bars, to prolong the ramp-in period of the strain wave (so called "ringing effects"), to achieve a dynamic equilibrium in a shorter time and to optimize the strain-rate. Specialized sensors based on quartz technology have been employed for precise force measurements directly at the faces of the specimen [42]. Low impedance visco-elastic bars have been used for the better impedance matching of the bar with the specimen [43–45] and specific calibration and wave time-shifting methods have been developed to process the signals from the visco-elastic bars [46]. Various wave separation techniques have been introduced to extend the experiment duration [47–51].

Special attention has been paid to the development of the specialized Hopkinson bar experimental setups optimized for testing of low impedance and cellular materials [15]. The experimental techniques often combine the specialized apparatus together with the aforementioned approaches. A long pre-loaded bar has been used instead of the conventional striker to develop very long incident strain waves and to compress the specimens of metal foam up to densification [16,52]. Important improvements have been made related to the application of direct impact Hopkinson bar [53] (DIHB) for the testing of cellular materials. DIHB has been employed for the testing of metal foams at high impact velocities [17,54,55] and has overcome a number of limitations of the conventional experimental setups. In DIHB, the specimen can be easily deformed to large strains (up to densification in the case of cellular solids), while the strain waves propagating in the setup do not exhibit disproportional amplitudes and are similar to each other. Moreover, DIHB can be used for the testing of cellular solids at high impact velocities as plateau stresses of the specimens are much lower than that of the bars. Therefore, the strain wave generated at the specimen-bar interface cannot induce plastic deformation in the bars. Both variants of the DIHB represented by the forward DIHB (FDIHB) and reverse DIHB (RDIHB) has been used for the testing of cellular materials [17,19,56], additively manufactured lattice structures [57,58] and to investigate shock effects in the material [54,59]. In FDIHB, the specimen is mounted on the instrumented transmission bar and is directly impacted by a projectile. The RDIHB is, in fact, a variant of the Taylor anvil test [60,61], where the specimen that is mounted on a projectile is launched against the instrumented transmission bar. However, as the DIHB is instrumented only on either side of the specimen, the equilibrium of the dynamic forces and strain of the specimen cannot be directly analyzed from the signals recorded at the transmission bar. This represents one of the limiting factors of the DIHB testing. The problem can be partially overcome by the combined testing using FDIHB and RDIHB [19], while the FDIHB is used to investigate the force histories on the back-side of the specimen and RDIHB is used for the same analysis on the impact-side of the specimen. This approach has two limitations: (i) it is considered that the wave propagation effects and dynamic forces are similar for all the tested specimens, (ii) the specimen has to fit into the barrel of the gas-gun. Therefore, this method cannot be employed for the testing of large specimens and/or specimens that are difficult to produce in large numbers like, e.g., additively manufactured panels. With the single-sided instrumentation, the strains are often evaluated using high-speed camera images.

A few research groups have investigated the methods for the two-sided instrumentation of the DIHB setup. A DIHB instrumented on both the incident bar (striker) and the transmission bar using a thin PVDF (polyvinyl fluoride) film gauges has been used for the testing of soft materials like rubber [62]. Another approach using photon Doppler velocimetry (PDV) has been tested in DIHB [63] to evaluate the velocity and force histories for both bars according to the PDV technique developed for SHPB [64]. The approach described in [62] has been tested at low velocities (up to approximately $10\,\mathrm{m{\cdot}s^{-1}}$). Although the PVDF gauges have a low noise and can produce smooth clear signals, their mounting is demanding and requires careful calibration to prevent stress concentrations at the contact. The method described in [63] has been employed on the direct impact testing of metal foams [65]. While it was demonstrated that the PDV instrumentation can be used even at velocities of approximately $100\,\mathrm{m{\cdot}s^{-1}}$ [63], some limitations arise from the demanding evaluation, flexural waves compensation and expensive instrumentation. Furthermore, problems with the laser beam positioning under the angle with the longitudinal axis of the striker bar, the weak reflected signal and mounting of the reflective pattern or coating on the striker bar complicate the application of the PDV method for measurements with large striker bar displacements. An advanced approach using the in-situ deceleration measurement has also been tested [66]. In this method, the striker bar instrumented with an accelerometer is employed to directly impact the specimen. As in the PDV based method, the technique can be used for the high velocity compression of the tested material. However, as the accelerometer is used as a sensor, extensive filtering of the measured signals has to be performed to estimate the forces and velocities during the impact. Another DIHB setup was proposed by Govender and Curry [67]. In the paper, the setup has been called the Open Hopkinson Pressure Bar (OHPB). The OHPB setup is, in principle, the DIHB instrumented by conventional strain-gauges on both bars. It was demonstrated that the technique is simple and with many benefits suitable for the testing of low impedance materials. The setup was tested via compression tests of a SAN (styrene acrylonitrile) foam using PMMA (poly-methyl methacrylate) bars with a diameter of 20 mm at impact velocities of up to $10\,\mathrm{m{\cdot}s^{-1}}$. The conventional SHPB setups can be relatively easily adapted to the OHPB variant, while standard strain-gauges can still be used as the instrumentation. As the PDV based method requires complex instrumentation and data processing, the in-situ deceleration technique requires an extensive filtering of the input signal and the applicability of

the other methods has been demonstrated at low velocities only, thus, the further experimental investigation of the performance and application envelope of the OHPB method is desired. Moreover, testing at low impact velocities (i.e., a relatively long impact duration) up to high strains, particularly with linear elastic bars (e.g., aluminum alloy) is complicated by the fact that the wave superposition occurs early at the strain-gauge location. In this case, the situation is worse for the incident bar, where the mounting of the second strain-gauge at the end of the bar is problematic. The second strain-gauge is necessary for the standard wave separation according to, e.g., [51].

In this paper, we introduce a different version of the OHPB setup than presented in [67]. A linear guidance system is employed to guide the incident bar during its acceleration provided by a gas-gun. With this arrangement, it is possible to achieve higher impact velocities without any bar alignment problems, parasitic bending and damage to the strain-gauges or wiring. The system has been successfully tested at impact velocities of up to approximately $30\,\mathrm{m{\cdot}s^{-1}}$. However, we are convinced that, with a higher performance of the gas-gun, this limit can be increased even further. DIC is used as a tool for the verification of the straight-forward wave separation technique requiring only a single strain-gauge at each bar allowing for the extension of the experimental time window several times. The experimental method has been tested with mid-sized linear elastic bars made of a high strength aluminum alloy and with visco-elastic bars made of PMMA. It is shown that, under certain circumstances, a simple linear elastic model is sufficient to perform measurements with the visco-elastic bars, while no additional attenuation and phase-shift corrections are necessary. The methods of the wave separation, the setup calibration and the DIC analysis are described in detail. The applicability of the experimental method is demonstrated on various experiments with conventional metal foams, hybrid foams, and additively manufactured auxetic lattices subjected to dynamic compression. Thus, the presented OHPB and methodology represent an interesting alternative to the testing of low impedance materials using the standard DIHB or SHPB that can be easily adapted, provides reliable results and uses standard instrumentation. The method is particularly beneficial for experiments, where instrumented striker bar is critically required together with the large strain in the specimen, i.e., the dynamic indentation of large specimens or panels that cannot be launched against an instrumented transmission bar in RDIHB.

2. Materials and methods

2.1. Open Hopkinson pressure bar

The principle of the OHPB method is directly derived from the DIHB methods. The schemes of both the forward and reverse DIHB method and the OHPB are shown in Fig. 1. Note that in the forward and reverse DIHB, only the transmission bar is instrumented with a strain-gauge. The OHPB consists of two measurement bars (incident and transmission) both of which are instrumented with strain-gauges. The incident bar is inserted into the barrel of the gas-gun and simultaneously serves as the striker bar. The specimen is mounted on the impact face of the transmission bar. During the experiment, the incident bar is accelerated using the gas-gun and directly impacts the specimen (see Videos S1 and S2). At the impact, the strain waves are generated in both bars. The pulses propagate from the specimen to the free ends of the bars. Then, the pulses are reflected and travel back to the specimen. The experiment ends (in the classical representation [67]) when the backward-propagating waves reach the strain-gauges, thus, producing superposed signals. As the waves propagate from the specimen, they have an approximately identical shape. The beginning of the transmission pulse is delayed in comparison with the incident pulse as the strain wave has to pass through the specimen (similarly to the SHPB).

Using the strain-gauge signals, it is possible to calculate the forces and displacements on the respected faces of the bars [67]. The forces on the incident face $F_{\mathrm{in}}(t)$ and on the transmission face $F_{\mathrm{out}}(t)$ can be calculated according to the relations

$$F_{\mathrm{in}}(t) = A_{\mathrm{in}} E_{\mathrm{in}} \varepsilon_{\mathrm{in}}(t), \tag{1}$$

$$F_{\mathrm{out}}(t) = A_{\mathrm{out}} E_{\mathrm{out}} \varepsilon_{\mathrm{out}}(t), \tag{2}$$

where A_{in}, A_{out} represent the cross-sectional area of the (input and output) bars, E_{in}, E_{out} represent Young's modulus of the individual bars and $\varepsilon_{\mathrm{in}}(t)$, $\varepsilon_{\mathrm{out}}(t)$ are the measured strain-gauge signals. The particle velocities $v_{\mathrm{in}}(t)$, $v_{\mathrm{out}}(t)$ at the ends of the bars can be represented using the relations

$$v_{\mathrm{in}}(t) = C_{0_{\mathrm{in}}} \varepsilon_{\mathrm{in}}(t), \tag{3}$$

$$v_{\mathrm{out}}(t) = C_{0_{\mathrm{out}}} \varepsilon_{\mathrm{out}}(t), \tag{4}$$

where $C_{0_{\mathrm{in}}}$ and $C_{0_{\mathrm{out}}}$ are the wave propagation velocities in the bars. By adopting the aforementioned formulas, the actual impact velocity $v(t)$ and the distance between the bars (or actual specimen length) $l_{\mathrm{s}}(t)$ are given by

$$v(t) = v_0 - C_{0_{\mathrm{in}}} \varepsilon_{\mathrm{in}}(t) - C_{0_{\mathrm{out}}} \varepsilon_{\mathrm{out}}(t), \tag{5}$$

$$l_{\mathrm{s}}(t) = l_0 - \int_0^t v(t)\mathrm{d}t = l_0 - \int_0^t (v_0 - C_{0_{\mathrm{in}}} \varepsilon_{\mathrm{in}}(t) - C_{0_{\mathrm{out}}} \varepsilon_{\mathrm{out}}(t))\mathrm{d}t, \tag{6}$$

where l_0 is the initial length of the specimen and v_0 is the initial impact velocity. Note that the evaluation of the actual length of the specimen (strain) is strongly dependent on the initial impact velocity v_0. Thus, in the OHPB, it is crucial to measure the velocity with high precision (by, e.g., DIC), unlike in the SHPB method, where the impact velocity serves as a secondary parameter useful for the verification of the results.

All the above described equations are valid for linear elastic bars. For experiments with visco-elastic bars, one of the well-known methods based on the propagation coefficient and the time-shifting in frequency domain [46,47,49,51] can be used. However, as it is demonstrated further in the text, under certain strict conditions, the linear elastic model can be adopted even for visco-elastic bars (see Section 2.4.4).

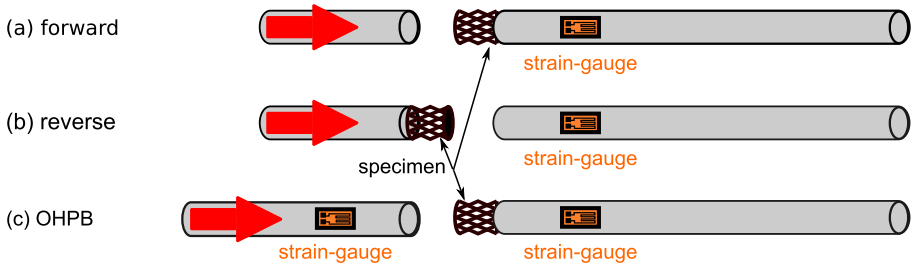

Fig. 1. Principle of the forward DIHB (a), reverse DIHB (b), and OHPB (c).

2.2. Digital image correlation

Digital Image Correlation (DIC) is an optical method employing tracking techniques for the measurements of the changes in the images. In this paper, an in-house developed software tool is employed for the tracking of the pseudo-random black-and-white speckles mounted on the bars and for the evaluation of the particle velocities at the faces of the bars. With the DIC tool, the tracking is achieved with a sub-pixel precision. First, the correlation is evaluated at the pixel level using template matching employing the Sum of Squared Differences (SSD) method. To obtain the sub-pixel precision, the pixel level difference is interpolated using a third order bivariate spline over the pixel grid. The best match is in the position of the minimum difference. The minimum of the difference (best match) is then found by minimizing the interpolated bivariate spline using the LM-BFGS algorithm.

2.3. Wave separation technique

The equations described in Section 2.1 are valid only until the strain wave is reflected at the free-end of the bar and it arrives back to the strain-gauge location producing the superposed signals. This situation is represented by the wave propagation diagram in Fig. 2(a). From this moment, the recorded signal is composed of a sum of forward- and backward-propagating strain waves. According to standard one-dimensional wave propagation theory, the actual particle velocity $v(t)$, and the actual force $F(t)$ at a certain cross-section of the bar are given by [51]

$$\varepsilon(t) = \varepsilon_F(t) + \varepsilon_B(t), \tag{7}$$

$$v(t) = c_0(\varepsilon_F(t) - \varepsilon_B(t)), \tag{8}$$

$$F(t) = EA(\varepsilon_F(t) + \varepsilon_B(t)), \tag{9}$$

where $\varepsilon_F(t)$ is the forward-propagating strain-wave and $\varepsilon_B(t)$ is the backward-propagating strain-wave. Wave separation methods for the decomposition of the forward- and backward-propagating waves in SHPB have been developed and are available [47,49,51]. The methods usually separate the waves using signals from at least two strain-gauges (or a strain-gauge and velocity sensor for a bar with a free-end) and are applicable even for visco-elastic bars. For the SHPB, a wave separation technique based on a single-point measurement and known boundary conditions was published in [50]. This method works without any redundant data source and does not account for the wave dispersion. In the case of the OHPB, the application of a second strain-gauge or direct velocity sensor would be complicated for the incident bar. Therefore, under certain circumstances, a simplified wave separation technique requiring only a single strain-gauge on each bar can be employed, while, in our case, its output is verified using DIC.

The straight-forward wave separation technique can be used if the following assumptions are satisfied:

- The waves propagate from the specimen to the free-ends of the bars.
- The free-ends are not in contact with other parts of the setup.
- The waves are generated directly at the interface between the specimen and the bar.
- The specimen has the lowest mechanical impedance in the experimental setup and deforms plastically up to a large strain.
- High frequencies are not present in the strain pulse as they are attenuated by the plastic deformation of the specimen.
- The wavelengths present in the strain pulse are several times higher than the diameter of the bar. Thus, the wave attenuation and dispersion effects can be neglected.

Under the aforementioned circumstances, a boundary condition valid for the free-end of the bar can be used to separate the individual waves. According to this boundary condition, the force at the free-end of the bar has to be zero. Thus, the waves at the free-end of the bar have to satisfy the following relations (see Fig. 2(b))

$$\varepsilon_F(t) + \varepsilon_B(t) = 0, \tag{10}$$

$$\varepsilon_B(t) = -\varepsilon_F(t). \tag{11}$$

According to the diagram shown in Fig. 2(a) the experiment begins at time $t = -\Delta t_s$ and the strain wave arrives at the strain-gauge location at time $t = 0$. Then, the time required for the wave to travel through the bar to its free-end is equal to Δt_e. Thus, at time $t = 2\Delta t_e$ the superposed signal is recorded by the strain-gauge and the measured signal $\varepsilon(t)$ is composed of two waves $\varepsilon_F(t)$ and $\varepsilon_B(t)$. By adopting the equations from above, the forward- and backward-propagating waves can be separated and are given by

$$\varepsilon_B(t) = -\varepsilon_F(t - 2\Delta t_e), \tag{12}$$

$$\varepsilon_F(t) = \varepsilon(t) - \varepsilon_B(t) = \varepsilon(t) + \varepsilon_F(t - 2\Delta t_e). \tag{13}$$

Using the procedure shown in Fig. 2(b), the relevant forward- and backward-propagating waves can be time-shifted to the bar-specimen interface producing strain waves $\varepsilon_{FS}(t-\Delta t_s), \varepsilon_{BS}(t-\Delta t_s)$ at the specimen's location and can be used to calculate the particle velocity $v(t-\Delta t_s)$ and the contact force $F(t-\Delta t_s)$ using the relations

$$\varepsilon_{FS}(t - \Delta t_s) = \varepsilon(t) + \varepsilon_F(t - 2\Delta t_e), \tag{14}$$

$$\varepsilon_{BS}(t - \Delta t_s) = -\varepsilon_F(t - 2\Delta t_e + \Delta t_s), \tag{15}$$

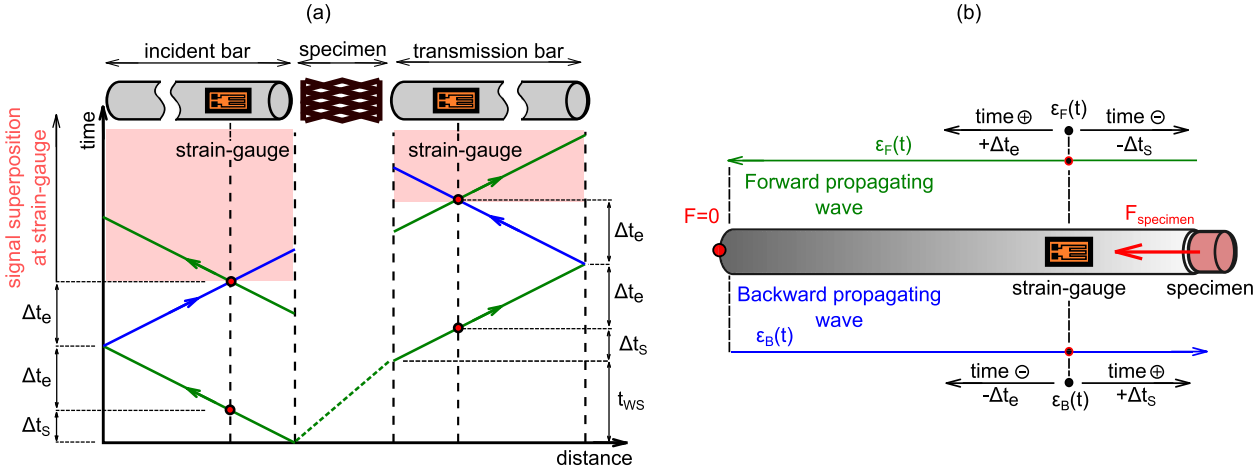

Fig. 2. Diagram showing the strain wave propagation in the OHPB setup (a). Principle of the wave separation and time-shifting (b).

$$v(t-\Delta t_s) = c_0(\varepsilon_{FS}(t-\Delta t_s) - \varepsilon_{BS}(t-\Delta t_s)), \quad (16)$$

$$F(t-\Delta t_s) = EA(\varepsilon_{FS}(t-\Delta t_s) + \varepsilon_{BS}(t-\Delta t_s)). \quad (17)$$

As the wave dispersion effects can be considered negligible, the waves can be separated using this procedure. Neither the shape nor amplitude of the waves needs to be updated. At the beginning of the experiment, the strain-gauge signal $\varepsilon(t)$ is not superposed between time $t = -\Delta t_s$ and $t = 2\Delta t_e$. Thus, this part of the pulse can be used for the iterative reconstruction of the signal.

In the real bars, the wave dispersion effects are always present and the strain wave is attenuated over time. Therefore, it is necessary to check whether the wave separation technique still produces reliable results. For this purpose, pseudo-random black-and-white speckle patterns are mounted on the bars as close to the specimen as possible. The high-speed camera is used to observe the specimen during the experiment, while the speckle patterns are observed together with the specimen. DIC is used to evaluate the displacements at the boundaries between the bars and the specimen. The displacements are calculated from the strain-gauge data by integration of the indicated velocities producing smooth curves (typically monotonous), where difference between the DIC and strain-gauges is represented by typically marginally different slopes of the curves. Conversely, the particle velocities of the bars' faces are calculated from the DIC displacements by differentiation. By its nature, differentiation brings more noise into the resulting velocity signal. Thus, a comparison of velocities is more difficult, but it is more useful to identify possible errors in the measurement and, if successful, produces more representative results. If the setup and DIC are properly calibrated, the particle velocities indicated by DIC have to be comparable with the velocities indicated by the separated strain-gauge signals time-shifted to the bar-specimen interface. The strain calculated without the wave separation plotted against time is compared with the strain calculated using the wave separation technique in Fig. 3(a). The velocities indicated by strain-gauges calculated without the wave separation and with the wave separation are compared with the velocity evaluated by the DIC in Fig. 3(b). Results of the wave separation technique in the incident bar of the OHPB are shown in Videos S3 and S4.

The wave separation technique, in this form, does not account for the wave dispersion effects including the attenuation and phase-shift. Therefore, it is not possible to use it for the visco-elastic bars. In the OHPB, the wave travel distance is usually long (typically close to 3 m for the experiments presented in this paper) because the strain wave has to propagate to the free end of the bar and then return back to the location of the strain-gauge. Thus, in the case of the visco-elastic bars, the backward propagating wave is significantly attenuated and phase-shifted. As a result, the assumption that the forward-propagating wave can be directly used for the wave decomposition does not hold true. However, a simple analysis valid until the wave superposition (see Section 2.1) can be used even for visco-elastic bars. Comparing typical materials used for visco-elastic and linear elastic bars in the Hopkinson bar devices (with the same length and configuration of the bars), a longer time window prior to the wave superposition is available for the visco-elastic materials because of their lower wave propagation velocities. For instance, the wave propagation velocity in aluminum alloy bars is approximately 5100 m·s^{-1}, while the wave propagation velocity for the PMMA is approximately 2100 m·s^{-1}. Therefore, approximately 2.5× longer time window is available for the PMMA compared to aluminum before the backward-propagating strain wave hits the strain-gauge producing superposed signals.

2.4. Setup calibration

The setup calibration is an important task that has to be carried out prior to every set of experiments. During the calibration procedure, the response of the strain-gauges is tested using a quasi-static force calibration. Furthermore, the behavior of the strain-gauges and DIC is compared in a series of dynamic void tests.

2.4.1. Quasi-static calibration

During the quasi-static calibration, the bars of the setup are subjected to an uni-axial compression using a piston mounted at the end of the experimental setup. A conventional membrane load-cell (U9B, HBM, Germany) is mounted co-axially between the bars (as the specimen). The values of the force calculated from the strain-gauges (and the known material properties of the bars) are compared with the force indicated by the load-cell. Using the quasi-static calibration, the proper functionality and precision of the strain-gauges are verified. Typically, the error of an individual pair of foil strain-gauges is up to 2 − 4% of the load-cell force.

2.4.2. Dynamic void tests

A void test is, in principle, an OHPB experiment without any specimen. The incident bar is accelerated using the gas-gun and directly impacts the transmission bar forming an elastic collision between two bars. Under such conditions, the kinetic energy of the incident bar is transferred to the transmission bar, while the duration of the collision corresponds to $2l/C_0$ in the case when both bars are made of the same material with the nominal wave propagation velocity C_0 and have the same length l. In such a theoretical case, the initial impact velocity v_0 of the incident bar decreases to $v_0/2$ during the collision. After the collision, the incident bar has zero velocity, while the transmission bar is

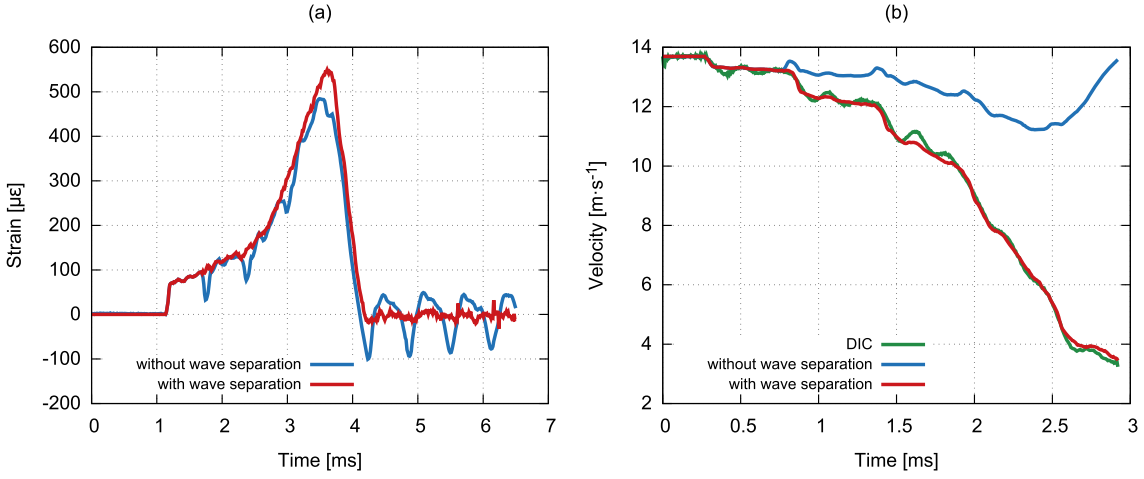

Fig. 3. Strain calculated without the wave separation plotted against time compared with the strain calculated using the wave separation (a). The velocities indicated by the strain-gauges calculated without the wave separation and with the wave separation compared with the DIC (b).

accelerated to v_0. During the void test, the strain-gauge signals are compared with the velocity obtained from the DIC and with the theoretical velocity value estimated according to the elastic collision theory. In the case of linear elastic bars, the error has to be maximally in the order of a few percent (typically better than $1-3\%$). The situation is more complicated for visco-elastic bars, however, the strain-gauge signals still have to closely correspond to the values obtained from the DIC (where an average difference approaching $6-10\%$ is considered to be an unacceptable error).

2.4.3. Linear elastic bars

The dynamic material properties, wave propagation velocity and dispersion of the bars are investigated according to method published by Bacon [46] using the "bars together" void test. The impact of the short striker colliding with the incident bar directly in the barrel of the gas-gun is used to evaluate the required parameters. For linear elastic bars, the results of the quasi-static calibration should closely match the outputs of the dynamic testing. Then, a set of dynamic void tests is performed, while the consistency of the strain-gauge signals is investigated. The velocities indicated by strain-gauges have to closely match the velocities evaluated using the DIC. Result of the quasi-static calibration of the high-strength aluminum alloy bars is shown in Fig. 4(a). The velocities indicated by the strain-gauges and DIC during the void test are compared in Fig. 4(b).

2.4.4. Visco-elastic bars

The situation is more complicated for visco-elastic bars. In this case, during the quasi-static calibration, the quasi-static material parameters have to be used to compare the strain-gauge signals with the load-cell. Then, the "bars together" void test is performed similarly as in the case of the linear elastic bars and the dynamic material properties of the visco-elastic model are evaluated according to [46]. Then, a set of dynamic void tests is used to compare the response of the strain-gauges with the DIC and with the theory of the elastic collision. The result of the quasi-static calibration of the PMMA bars is shown in Fig. 5(a). The velocities indicated by the strain-gauges and DIC during the void test are compared in Fig. 5(b).

Conventionally, the waves in the visco-elastic bars have to be time-shifted in the frequency domain using the visco-elastic material model and a function of the wave propagation coefficient [46]. However, in the case of the OHPB, simplifications can be adopted if the following testing conditions are satisfied:

- The strain-gauges are mounted as close as possible to the specimen. Proximity of the sensors to the location of the impact ensures that the recorded signals are highly similar to the original signals generated by the impact.
- The amplitudes of the strain waves are low in comparison with the theoretical strain capacity of the bar at a given impact velocity. For the small strain amplitudes, non-linear effects in the polymeric bars are significantly suppressed, while the distortion becomes more severe with the increasing amplitudes.
- The wavelengths of the frequencies present in the recorded pulses are several times higher than the diameter of the bars. This assumption is essential for significant reduction of the wave dispersion effects during the experiment.
- The specimen deforms plastically and acts as an effective filter of the higher frequencies. Plastic collapse of the specimen prevents transfer of high frequencies that are significantly affected by the wave dispersion effects.
- No significant bending is present during the testing. If significant bending is observed during the experiment, the specimen does not follow the uni-axial loading leading to more complex modes of deformation. Moreover, the measurement technique cannot compensate for a minor bending of the bars and the measured signals are distorted.

When the above described conditions are fulfilled, the time-shifting procedure can be processed identically as in the case of the linear elastic bars. Because the dynamic properties of some visco-elastic materials are approximately constant at lower frequencies for long projectiles (as presented in Fig. 6(a,b) for a projectile with a length of 1750 mm and a diameter of 20 mm made of PMMA), the average value of the complex modulus and the phase velocity for that can be used for the calculation of the particle velocity and the force, while the frequency domain based time-shifting of the signal is not necessary. The signals recorded by the strain-gauges at distances of 200 mm and 400 mm from the impact face of the PMMA bar with a diameter of 20 mm are time-shifted by the frequency domain method and compared with the output of this simplified approach in Fig. 7(a). It can be seen that, using this simple approach, the error caused by the wave attenuation is more profound with the increasing amplitude of the recorded signal, while the frequency domain time-shifting procedure can better compensate for this error. No significant phase-shift effects are observable in the presented example. The method for the dispersion correction in the visco-elastic bar based on the frequency domain approach produces more precise results. However, as the recorded amplitudes of the tested cellular materials are usually low and the effects of the attenuation and dispersion are small or negligible for the short travelled distance, the simple method can be adopted. As can be seen in Fig. 7(a), its error over

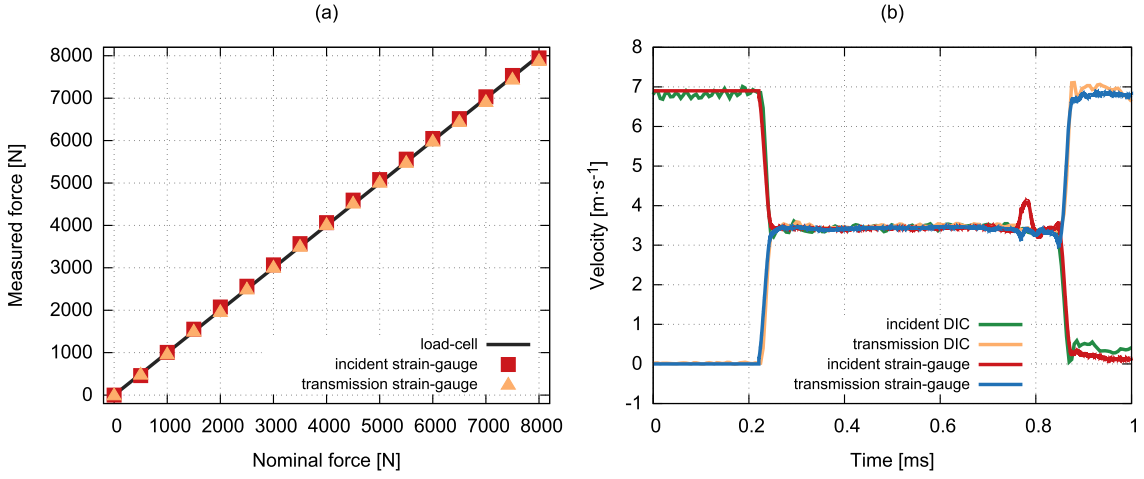

Fig. 4. Force indicated by the strain-gauges compared with the load-cell during the quasi-static calibration procedure, aluminum alloy bars (a). The velocities indicated by the strain-gauges during the void test compared with the DIC, aluminum alloy bars (b).

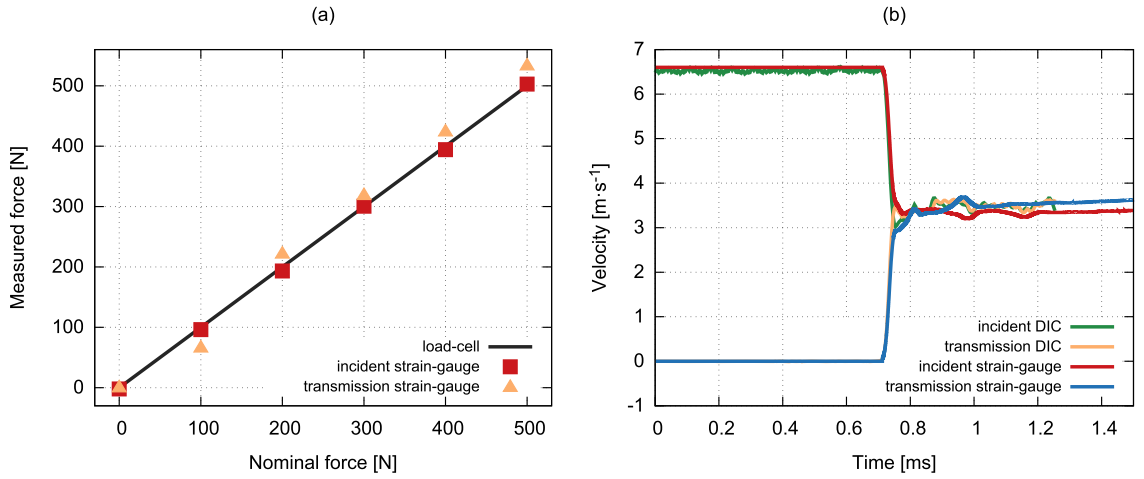

Fig. 5. Force calculated from the strain-gauge signals compared with the force value measured by the load-cell during the quasi-static calibration procedure, PMMA bars (a). The velocities calculated from the strain-gauge signals during the void test compared with values from the DIC, PMMA bars (b). Note that the DIC was not able to capture the separation of the bars as it happened out of the field of view due to the large displacements of the PMMA bars.

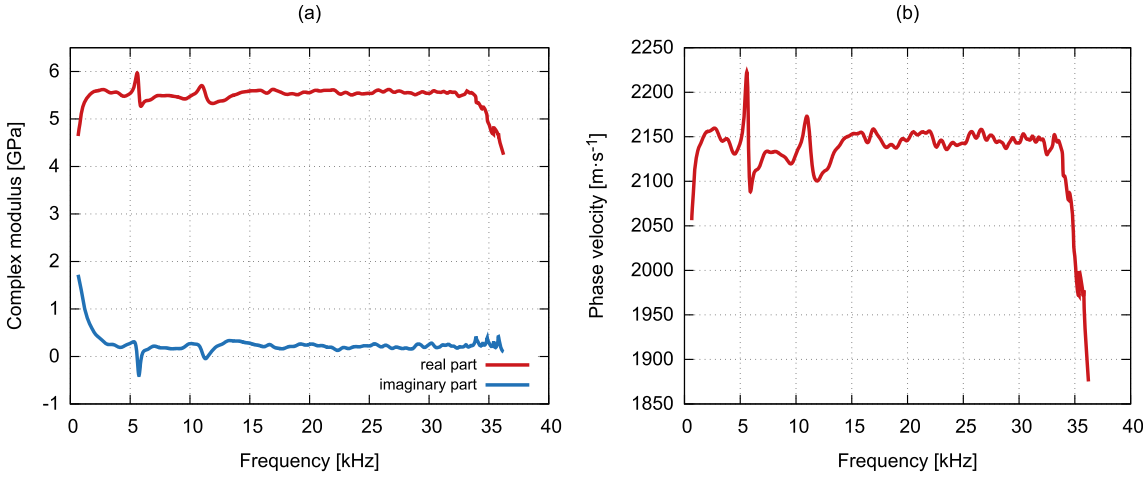

Fig. 6. Visco-elastic properties of the PMMA projectile with a length of 1750*mm* and a diameter of 20*mm* at an impact velocity of $7m{\cdot}s^{-1}$. Complex modulus (a). Note that the rapid changes in the low frequencies (approximately below 2*kHz*) are related to the conversion of the measured signal to frequency domain using Fast Fourier Transform and does not represent the actual material properties. The phase propagation velocity of the PMMA bars (b).

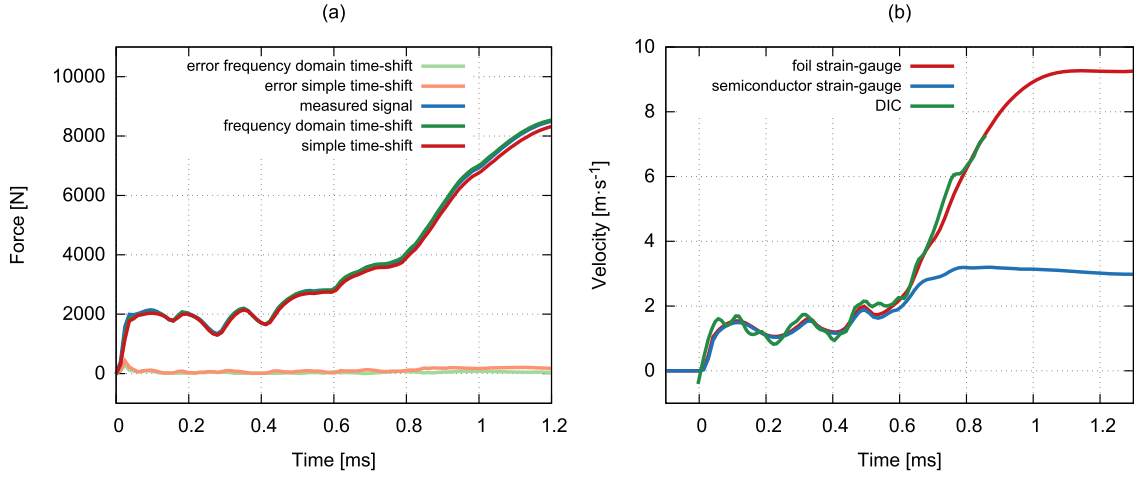

Fig. 7. Signals recorded by the strain-gauges at distances of 200*mm* and 400*mm* from the impact face of the PMMA bar with a diameter of 20*mm* time-shifted by the conventional frequency domain method compared with the output of the simplified approach (a). The velocity calculated using the data of the semiconductor (AFP-500-090, Kulite, USA) and foil (3/120, LY61, HBM, Germany) strain-gauge during the impact experiment compared with the DIC (b).

the 200 mm travel distance is negligible for forces of up to approximately 4000*N* and the error is around 2% at a force of approximately 8000*N*. Therefore, with care, this simple approach can be used to avoid problems caused by the inverse Fourier transform, where the errors or peaks in a function of the propagation coefficient can result in the reconstruction of distorted signals.

2.5. Experimental setup

In this paper, we present a set of representative results from the two-sided direct impact Hopkinson bar testing of conventional metal foams, additively manufactured auxetic lattices, and hybrid auxetic constructs. For the measurements, two variants of the OHPB experimental setup were used: (i) a setup with aluminum alloy bars of an identical diameter for the uni-axial compression testing, (ii) a setup with PMMA bars of an identical diameter for the uni-axial compression testing. Foil strain-gauges were used instead of the semiconductor strain-gauges due to their linearity, durability and longer service-life. The use of the semiconductor strain-gauges was rejected mainly because of their strongly non-linear response above approximately 500$\mu\varepsilon$ (see the velocity profiles evaluated from the semiconductor and foil strain-gauges compared with the DIC in Fig. 7(b)). Nevertheless, the semiconductor strain gauges were used as the auxiliary sensors with limited service-life in the selected experiments. The arrangement of the individual experimental setups is presented in Fig. 8.

2.5.1. Linear guidance system

In all the variants of the presented OHPB setup, a low mass/low friction linear guidance system was employed to guide the incident bar during the acceleration over a relatively long travel distance. The linear guidance system consisted of a linear motion guide with a high performance polymeric slider bearing (drylinT, IGUS, USA) and a rail with a length of 1200 mm. The incident bar was attached to the carriage via a friction contact clamp. The tightening moment of the clamp had to be kept constant for all the experiments and was re-adjusted after each impact. During the calibration testing, it was found out that the friction clamp did not bring any distortion to the incident wave if adjusted properly. As the design parameters of the used bearing type were partially outside the OHPB velocity envelope, the bearings had to be replaced after a certain number of measurements (usually after a few dozen impacts) due to wear and tear. The stiffness, performance and durability of the system could be probably further improved with the use of caged-ball linear motion guides optimized for high-speed applications.

2.5.2. Gas-gun system

An in-house gas-gun system was used for the acceleration of the incident bar. This system consists of a barrel with an inner diameter of 20 mm and a length of 2500 mm which is connected to a 20*l* air reservoir with a maximum operating pressure of 1.6 MPa. The compressed air is released by a solenoid valve (366531, Parker, USA).

2.5.3. High-speed imaging and data acquisition system

All the experiments were observed with high-speed camera(s). In the described experiments, two types of high-speed cameras were used: (i) Fastcam SA-5 (Photron, Japan), (ii) Fastcam SA-Z (Photron, Japan). A typical experiment was captured with the latter camera at 252*kfps* with an image resolution of $256 \times 168px$. The illumination of the scene was undertaken using a pair of high intensity LED lights systems: (i) Constellation 60 (Veritas, USA) and (ii) Multiled QT (GS Vitec, Germany). The strain-gauge signals were amplified by a pair of low-noise differential amplifiers (EL-LNA-2, Elsys AG, Switzerland) with a gain of 100 and recorded by high-speed digitizer cards (PCI-9826H, ADLINK Technology, Inc., Taiwan) operating at 20 MHz. The digitizer cards were synchronized with the high-speed camera(s) using a pair of short-reaction-time through-beam photoelectric sensors (FS/FE 10-RL-24 PS-E4, Sensopart, Germany) serving as a trigger and as a redundant method (together with DIC) for the estimation of the initial impact velocity. The data acquisition system was implemented in LabView software (National Instruments, USA).

2.5.4. Aluminum alloy bars

A high-strength aluminum alloy (EN-AW-7075-T6) was used as the material of the bars. Both bars had a length of 1600 mm. The bars were instrumented by a pair of foil strain-gauges (3/120, LY61, HBM, Germany) located at a distance of 200 mm from the impact faces arranged in a half-bridge circuit. The transmission bar was supported by low friction bearings (drylin TJUM series, IGUS, USA). Using this setup, the results summarized in Section 3.1 and 3.3 were acquired. The experimental setup with the aluminum alloy bars and the important parts of the OHPB arrangement are shown in Fig. 9.

2.5.5. PMMA bars

For the testing of the low impedance materials, the setup was fitted with PMMA bars with a diameter of 20 mm and a length of 1750 mm. The basic characteristics of the setup remained unchanged with only a few minor changes in the instrumentation. Semiconductor strain-gauges (AFP-500-090, Kulite, USA) with an active length of 2.29 mm were mounted together with the foil strain-gauges as redundant strain sensors. A single measurement point was mounted at the incident bar at a distance of 200 mm from the impact face. Two measurement points were mounted at the transmission bar at a distance of 200 mm and 400 mm from the impact face. Using this setup, the results summarized in Section 3.2 and 3.4 were measured. The OHPB setup with the PMMA bars during the experimental campaign is shown in Fig. 10.

3. Applications and results

The applications of the OHPB experimental setup and the representative results exploiting the important features of the direct impact Hopkinson bar with two-sided instrumentation are presented. The applicability and performance of the setup is demonstrated with the results of two different experimental campaigns: (i) the uni-axial high strain-rate compression of the additively manufactured auxetic lattices

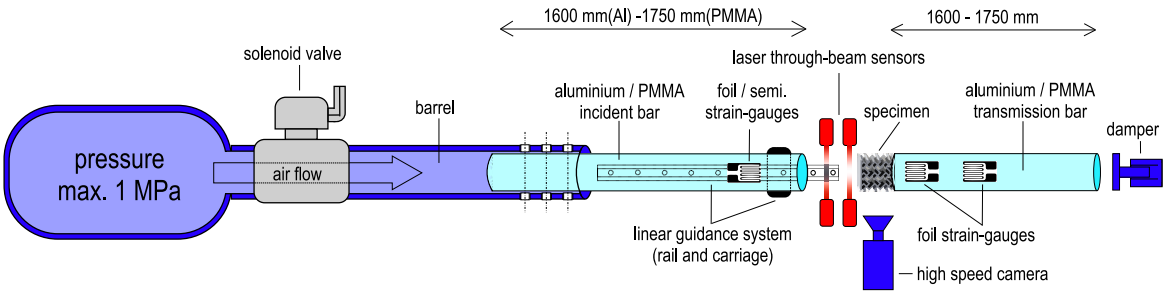

Fig. 8. The arrangement of the OHPB experimental setup: uni-axial compression with the aluminum alloy/PMMA bars.

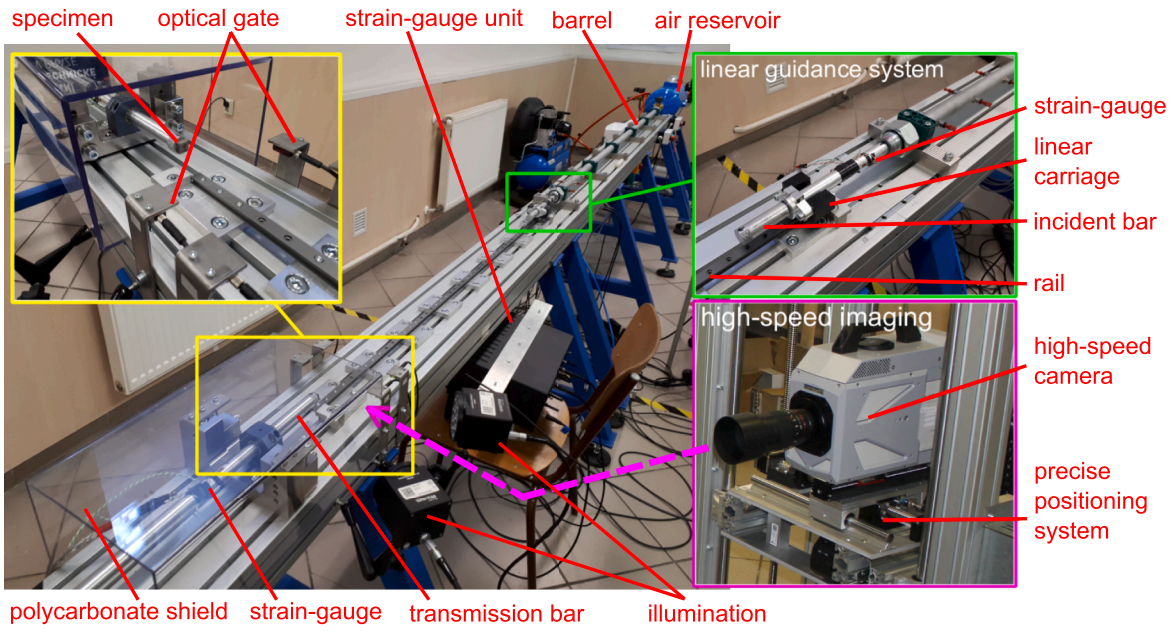

Fig. 9. The experimental setup with the aluminum alloy bars and the important parts of the OHPB arrangement.

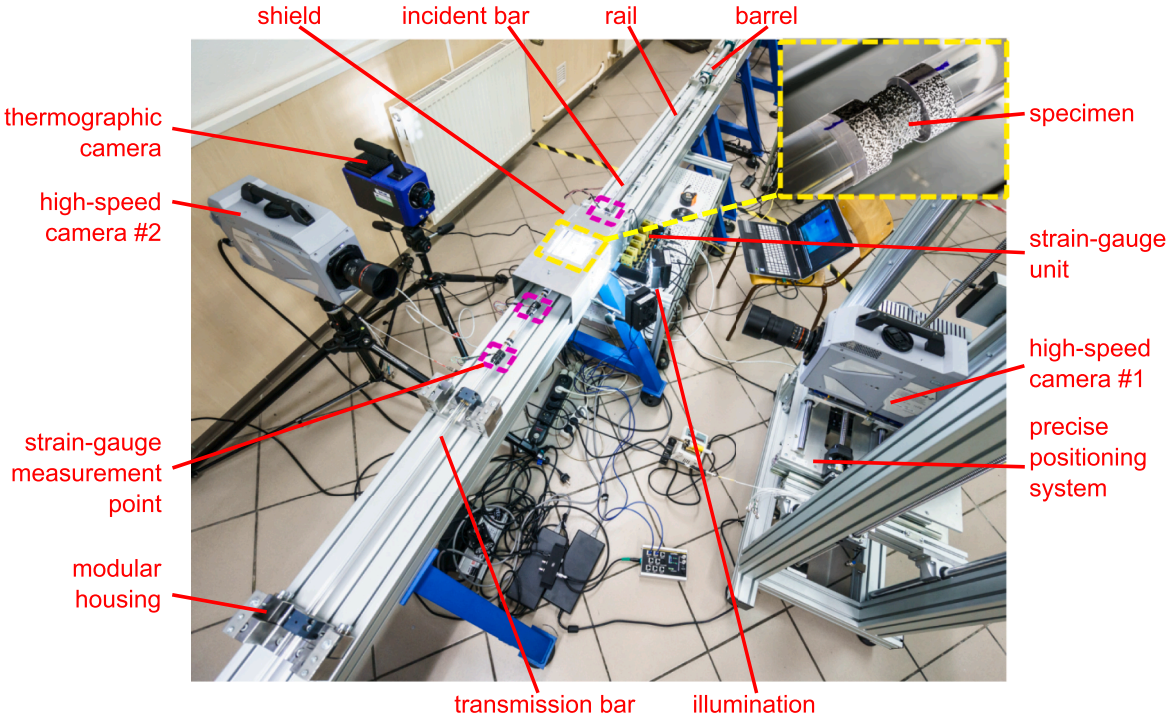

Fig. 10. The experimental setup with the PMMA bars during the experimental campaign.

and conventional metal foams, (ii) the uni-axial high strain-rate compression of the low impedance hybrid auxetic lattices. The range of impact velocities for every type of material was selected by taking multiple aspects into account. Besides the quasi-static response of the specimens, indicating on the stiffness, plateau stress, and densification strain, numerical simulations with the virtual OHPB apparatus developed in LS-DYNA were used to predict the deformation response of the specimens together with the performance of the setup including effective DIC measurement windows. The following sections show the representative results for different impact velocities selected according to the deformation characteristics of the particular tested material.

3.1. Closed-cell aluminum foam

Cubic specimens of the closed-cell aluminum foam with commercial name Alporas with a size of approximately 15 × 15 × 15mm, a density of 0.25-0.3 g ··· cm^{-3} and a porosity of 89% were tested with the aluminum bars. The material had a low mechanical impedance and exhibited localized strain bands in compression, where the majority of deformation was observed. A slideshow showing a specimen of Alporas foam during dynamic compression is presented in Fig. 11(a). The Alporas foam has already been tested by a number of research teams [68–71]. In this paper, we present the results showing the ability of the

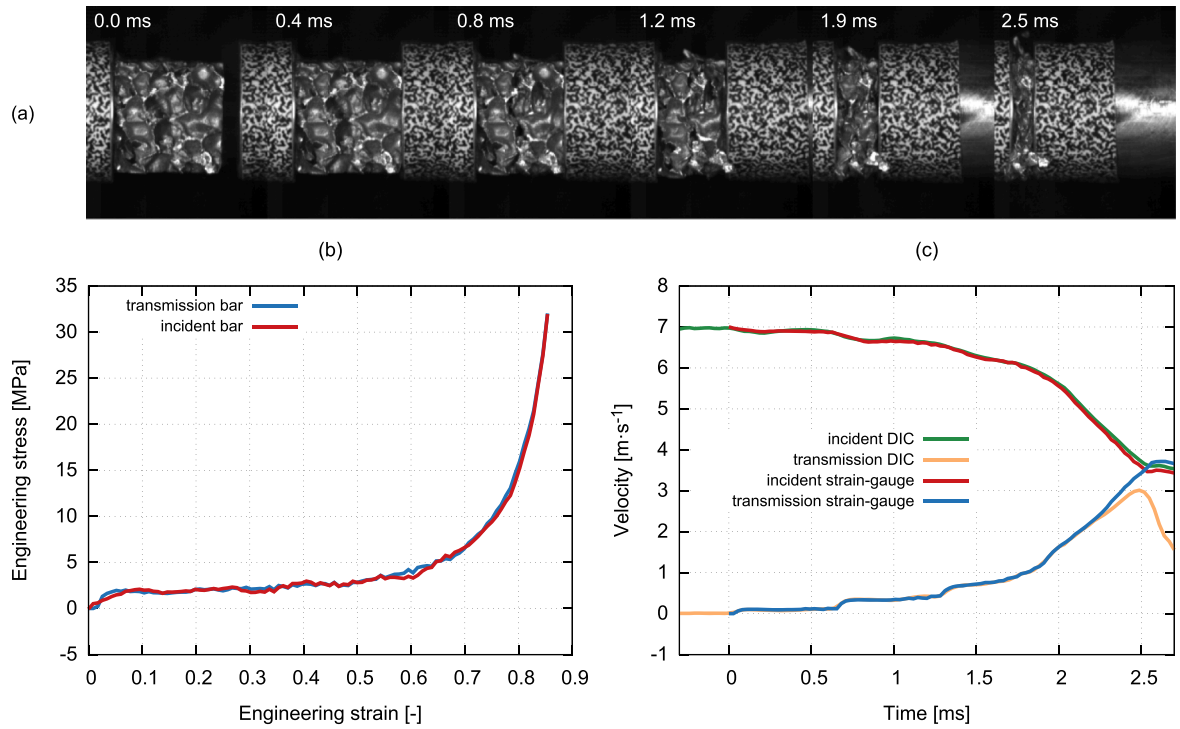

Fig. 11. Closed-cell Alporas foam, EN-AW-7075 bars. Slideshow showing a specimen of the Alporas foam in dynamic compression (a). Dynamic equilibrium and stress-strain diagram (b). Velocity profiles on both bars compared with the velocities from the DIC (c).

OHPB method to reliably capture the dynamic behavior of the foam with a very nice dynamic equilibrium. The dynamic equilibrium after wave separation is shown in Fig. 11(b). The wave separation technique produced precise results verified by the DIC. The velocity profiles on the both bars are compared with the DIC in Fig. 11(c). Impact into the Alporas foam recorded by the high-speed camera with mapped DIC results of the longitudinal displacement and incremental strain is shown in Videos S5 and S6.

3.2. Open-cell aluminum foam

Cubic specimens of an open-cell aluminum foam with a size of approximately $15 \times 15 \times 15$ mm, a density of $0.18 - 0.25\,\mathrm{g{\cdot}cm^{-3}}$ and a porosity of 93% were tested in dynamic compression using the OHPB with PMMA bars. As this foam has significantly lower mechanical impedance than the Alporas foam, the testing of such a material using the conventional setups is quite challenging. The force-displacement diagram recorded during the impact with an initial impact velocity of approximately $6.5\,\mathrm{m{\cdot}s^{-1}}$ is shown in Fig. 12(a). Note that the stress level at the initial part of the plateau region was approximately 0.2 MPa (corresponding to a force of approximately 100N in this case), while the dynamic behavior, oscillations of the incident stress, and its convergence with the transmission stress were clearly recorded. The velocity profiles on both bars compared with the DIC are shown in Fig. 12(b).

3.3. Additively manufactured auxetic lattices

Additively manufactured auxetic lattices (metamaterials with a negative Poisson's ratio) were manufactured using a selective laser sintering (SLS) method from SS316L powdered austenitic steel. Different

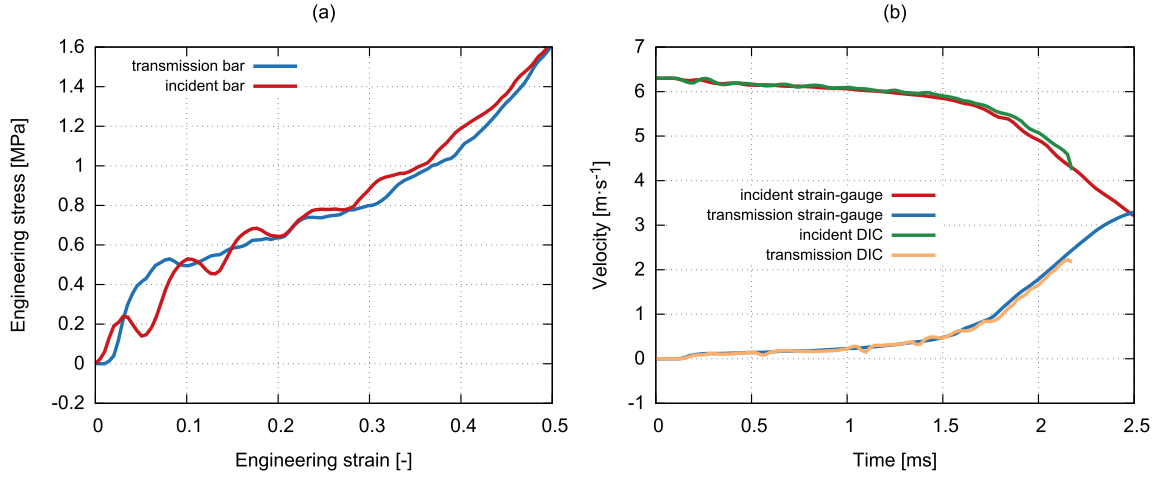

Fig. 12. Open-cell aluminum foam, PMMA bars. Stress-strain diagram recorded during the impact with an initial velocity of approximately $6.5 m{\cdot}s^{-1}$ (a). Velocity profiles on both bars compared with the DIC (b).

sizes and types of the auxetic lattices were tested in the experimental campaign. Both 2D and 3D auxetic structures were investigated: a 2D re-entrant honeycomb, a 3D re-entrant honeycomb, and a 2D missing-rib structure. Here, the representative results of the 2D re-entrant honeycomb are presented as this structure is considered very versatile [7]. The structure had nominal dimensions of $12.15 \times 12.15 \times 12.58$ mm, a density 3.32 g·cm^{-3} and a porosity of 59% with a nominal strut thickness of 0.3 mm which was at the resolution limit of the used SLS device (AM 250, Renishaw, UK). The 2D re-entrant construct with a detailed view from the scanning electron microscopy (SEM) of the printed strut is shown in Fig. 13(a). The representative velocity histories evaluated using the strain-gauges during the impact with an initial velocity of approximately 20 m·s^{-1} are compared with the DIC in Fig. 13(b). Note that the structure reached full densification and the final stage of the experiment corresponded to the elastic collision, where the velocities of the individual bars converged and the bars finally separated due to the reflected elastic waves. The wave separation technique was able to reliably separate the waves until the random speckle pattern mounted on the transmission bar disappeared from the images and the DIC tracking was no longer possible.

3.3.1. Dynamic crushing at different strain-rates

Special attention was paid to the analysis of the crushing behavior of the 2D re-entrant auxetic constructs. The specimens were subjected to impacts at two different velocities of 12 m·s^{-1} and 20 m·s^{-1}. With the increasing strain-rate, the auxetic lattice exhibited a different crushing behavior. The stress value, at which the collapse of the first layer of the auxetic structure occurred, increased with the strain-rate. Furthermore, the collapse mechanism of the individual layers was different as, during the impact at the lower velocity, significant lateral movements of the layers were observed with the corresponding peaks in the loading diagram. During the impact at the higher velocity, this effect was significantly suppressed as the inertia effects and the impact velocity acted against the lateral motion. The comparison of the deformation mechanism of the 2D re-entrant honeycomb lattice at the two different impact velocities is shown in Fig. 14(a,b). More importantly, the crushing mechanism was analyzed at both faces of the specimen using the two-sided instrumentation. As many stress oscillations occurred in the post-peak plateau region, the two-sided analysis of the phenomena was important. The stress-strain diagrams for both impact velocities and both faces of the specimen are compared in Fig. 14(c). Note that the velocity measured by the DIC closely followed the strain-gauge signals in every oscillation. Furthermore, the initial collapse was observed at a higher stress for the higher impact velocity and that the oscillations in the post-peak plateau had higher amplitudes at the lower velocity. Moreover, at the lower velocity, the stress oscillations on both faces of the specimen were approximately identical, whereas, at the higher velocity, the oscillations were delayed and/or attenuated. Also, at the lower velocity, the signals from both faces of the specimens intersected earlier than at the higher velocity showing that the behavior is related to initial wave propagation and convergence of the dynamic forces. The same structure was tested in our previous study [11,12] using an SHPB with copper pulse-shapers, a striker bar with a length of 500 mm and a similar overall length of the setup. The SHPB was used for the compression of the auxetic lattice at approximately the same impact velocity of $20 m \cdot s^{-1}$. While it was possible to compress the construct up to the full densification with the OHPB (nominal strain > 0.5), the maximum engineering strain in the SHPB was around 0.25. Even at the lower testing velocity of approximately 12 m·s^{-1}, the OHPB with the wave separation technique was able to reach maximum strain of 0.35-0.4. Velocity histories measured by the strain-gauges at both faces of the specimen are compared with the DIC for the impact with an initial velocity of approximately 20 m·s^{-1} in Fig. 14(d). Impact into the auxetic re-entrant lattice foam recorded by the high-speed camera with mapped DIC results of the longitudinal displacement and incremental strain is shown in Videos S7 and S8.

3.4. Hybrid auxetic lattices

Hybrid auxetic lattices represent a novel approach in the low-cost manufacturing of an advanced light-weight materials. In this work, the specimens were printed using a Pro Jet HD3000 3D printer (3D Systems, Rock Hill, USA) from a UV-curable polymer VisiJet EX200 with the highest resolution ($656 \times 656 \times 800$ dpi). The overall dimensions of the specimens were approximately $14 \times 14 \times 20 \times mm$ (width, depth, height). The polymeric samples were electro-chemically coated with an $\approx 60\,\mu$m and $\approx 120\,\mu$m thick layer of nickel, respectively. The average density of the samples was: (i) 0.27 g·cm^{-3} for the non-coated construct, (ii) 0.469 g·cm^{-3} for the $60\mu m$ coating, and (iii) 0.537 g·cm^{-3} for the $120\,\mu$m coating. Further information on the coating process can be found in [4]. After the coating, the polymer was taken out via pyrolysis at approximately $1000^{\circ}C$. The printed polymeric constructs as well as the final hybrid coated hollow-strut auxetic structures are shown in Fig. 15.

3.4.1. No coating

As the printed polymer was very brittle, the uncoated constructs disintegrated instantly after the initial impact. The disintegration captured by the high-speed camera is shown in Fig. 16(a). Nevertheless, the force measurement during the disintegration was possible with the OHPB method. The corresponding stress-strain diagrams showing the

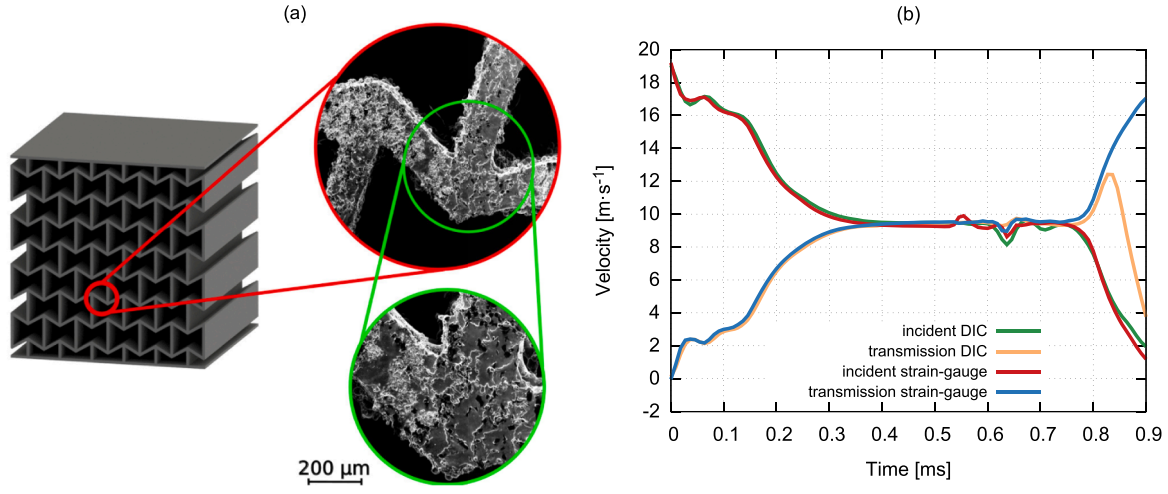

Fig. 13. The 2D re-entrant construct with an SEM detail of the printed strut (a). Velocity profiles on both bars compared with the DIC (b).

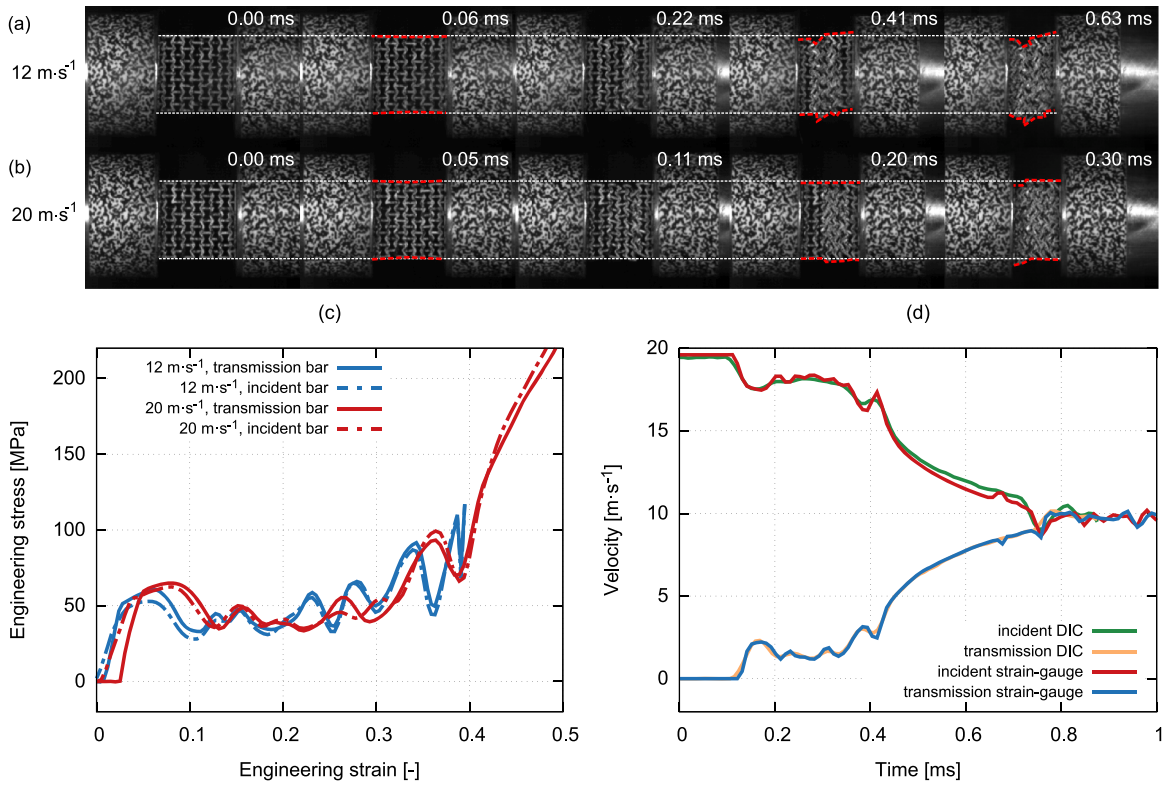

Fig. 14. Deformation mechanism of the 2D re-entrant lattice at two different impact velocities (a, b). Stress-strain diagrams at both impact velocities and both faces of the specimen (c). Velocity histories indicated by the strain-gauges at both faces of the specimen compared with the DIC for the impact with an initial velocity of approximately $20 m{\cdot}s^{-1}$ (d).

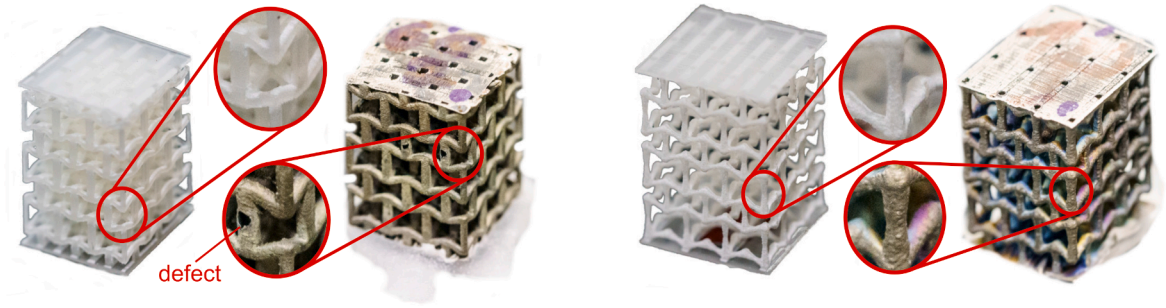

Fig. 15. The printed and coated hybrid auxetic constructs.

behavior at both faces of the disintegrating specimen are shown in Fig. 16(b). The velocity histories at both bars evaluated from the strain-gauge signals are compared with the DIC results in Fig. 16(c). Note that despite the very rapid disintegration, the short force peaks were recorded reliably and were comparable with the values from the DIC. This indicates that the wave dispersion in the PMMA bars over the short travelled distance in the OHPB was minor and the resulting force peaks were still relevant. The behavior after the disintegration when the bars hit the residuals of the specimen and underwent an elastic collision were also captured despite some discrepancy between the incident strain-gauge and the DIC, which can be identified as the wave separation in its simple form, as it cannot reliably account for the wave dispersion over long travel distances.

3.4.2. *Nickel coating - 60 μm*

The hollow-strut hybrid auxetic lattice with a coating thickness of 60 μm exhibited ductile behavior. The structure deforming during the impact is shown in Fig. 17(a). Note a very profound auxetic behavior with the struts rapidly closing into the core of the specimen. Stress-strain diagrams are presented in Fig. 17(b). The velocities evaluated from the strain-gauge signals are compared with the DIC in Fig. 17(c). Here, the perfect match of the strain-gauge velocities and the DIC is very important as the behavior of the specimen at the impacted face was different than at the opposite face. Interestingly, the incident curve was lower than the transmission curve up to the densification of the structure, where both curves converged. All the tested specimens with a coating thickness of 60 μm exhibited this behavior. As the incident curve did not exhibit any stress oscillations, the phenomenon could not be simply explained by the classical convergence of the dynamic forces. As the coating process is not perfect, the coated layer had a lot of imperfections, defects and cracks (see Fig. 15) affecting the response of the samples. The distal face of the specimen was embedded in a resin for the better contact with the transmission bar face, while the impacted face was without any embedding. Also, by design, the auxetic cells were not distributed symmetrically along the length of the specimen. These factors can possibly cause some distortion and/or internal reflections of the

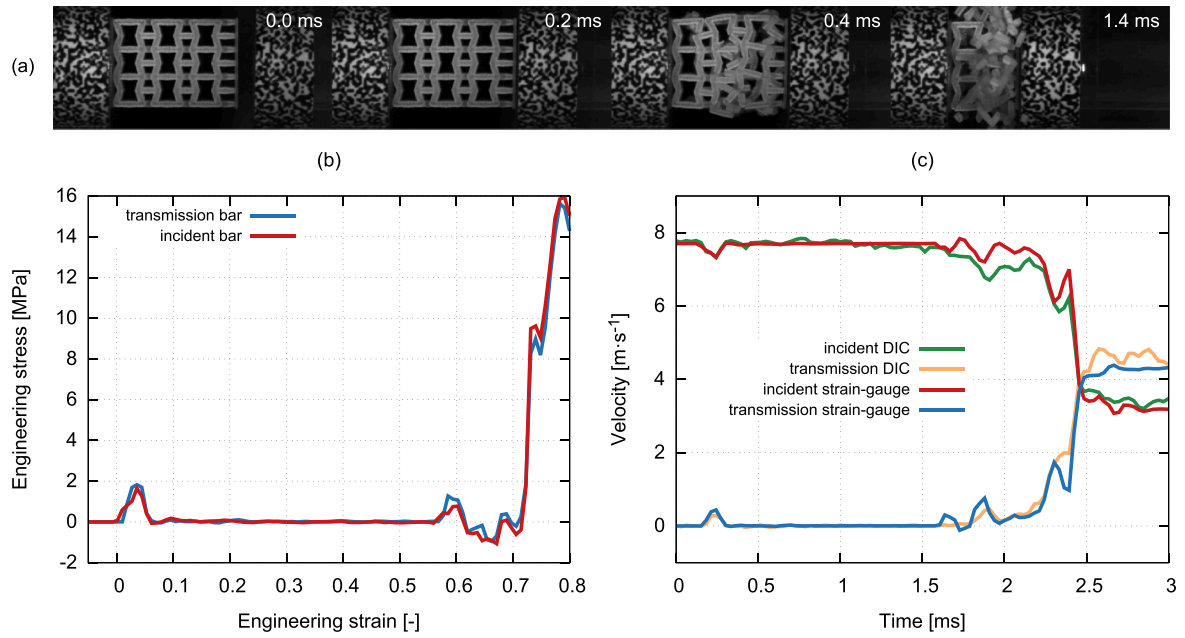

Fig. 16. The disintegration of the polymeric construct captured by the high-speed camera (a). Stress-strain diagrams showing the behavior at both faces of the disintegrating specimen (b). Velocity histories at both bars evaluated from the strain-gauge signals compared with the velocities from the DIC (c).

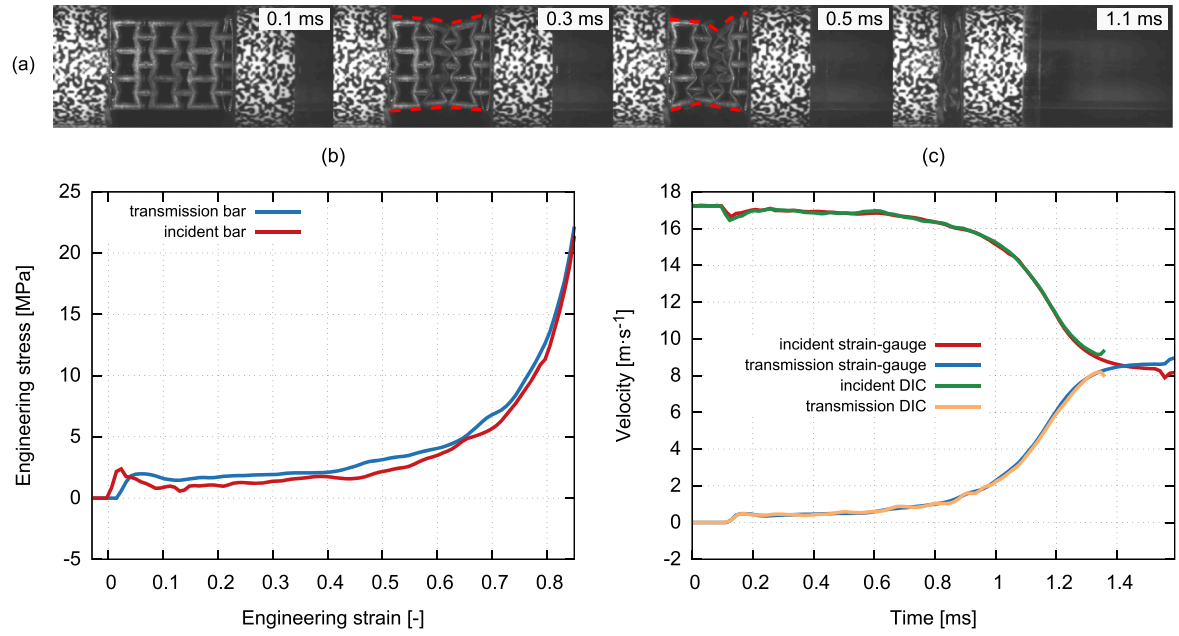

Fig. 17. The hybrid auxetic construct with a coating thickness of 60μm deforming during the impact (a). The corresponding stress-strain diagrams (b). Velocities evaluated from the strain-gauge signals compared with the DIC (c).

strain wave in the specimen or wave transfer problems that were represented by the asymmetrical response recorded by both the strain-gauges and the DIC. Furthermore, this effect was not observed in the case of the structures with a coating thickness of 120 μm, where the dynamic forces converged quickly (see Section 3.4.3).

3.4.3. *Nickel coating - 120 μm*

Hybrid auxetic lattices with a coating thickness of 120 μm were tested. In this case, the behavior was very different from the constructs with a coating thickness of 60 μm. Stress-strain diagrams showing a quick convergence of the dynamic forces at the respective faces of the specimen are shown in Fig. 18(a). The velocities evaluated using the strain-gauges and the DIC are shown in Fig. 18(b). Note that the DIC was able to track the image features and compute the velocity only for a short period of time. As these constructs exhibited a stiffer response, the speckle pattern mounted at the transmission bar quickly disappeared from the image making further tracking impossible. Impact into the hybrid auxetic lattices recorded by the high-speed camera with mapped DIC results of the displacements and incremental strains is shown in Videos S9 - S12.

4. Discussion

Several different types of cellular solids and lattices were tested using

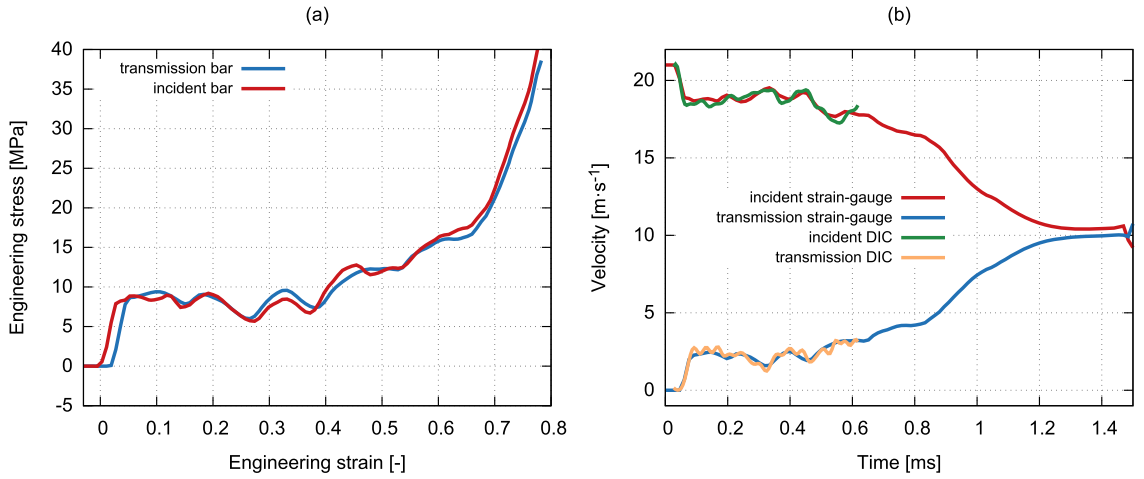

Fig. 18. The hybrid auxetic construct with a coating thickness of 120μm: The corresponding stress-strain diagrams (a). Velocities evaluated from the strain-gauge signals compared with the DIC (b).

the OHPB in dynamic compression. Based on the analysis of the acquired results, the following comments, findings and remarks can be drawn:

- The DIHB experimental setup instrumented with strain-gauges mounted on both the incident and the transmission bar (the so called OHPB [67]) with the linear motion guidance system supporting the incident bar can be successfully employed for impacts with an initial velocity of at least 30 $m{\cdot}s^{-1}$ (see representative diagrams in Fig. 19). In comparison with the similar previously published setups [62,67], the presented variant of the OHPB setup significantly extended the application envelope in terms of the maximum impact velocity (an impact velocity of 10 $m{\cdot}s^{-1}$ is mentioned as a reasonable maximum in the arrangement published in [67]). Moreover, the linear guidance system allowed for the easy installation of the strain-gauges and wiring that is more complicated in the variant with the incident bar and strain-gauge in the barrel of the gas-gun.
- The instrumentation with the conventional strain-gauges represents a straightforward approach for the evaluation of the results which is not different from the classical Kolsky bar measurements. This approach is simple and does not require expensive instrumentation such as the PDV. However, the PDV is simultaneously a type of instrumentation suitable for the testing at higher impact velocities [63]. Application of two strain-gauges at a single measurement point connected in a half Wheatstone bridge arrangement can compensate for the minor bending of the bars and effects of the flexural waves that can possibly occur during the testing of the specimens with a complex internal structure.
- No significant bar alignment problems were identified with the applied linear guidance system. After the careful adjustment and calibration of the experimental setup, no problems with the wave reflections from the friction clamp that attaches the incident bar to the linear guidance system occurred. The wear and tear of the polymeric linear bearings were observed particularly during impacts close to the maximum impact velocity. Thus, the bearings had to be replaced after a certain number of experiments.
- The wave separation technique based on the arrangement specific to the OHPB, where both bars have free-ends, was employed to separate the forward- and backward-propagating waves in the bars. This approach allowed the duration of the experiment to be extended several times.
- The DIC was used as a technique for the measurements of the displacements and the velocities in the vicinity of both faces of the specimen. DIC was also employed as a tool for the verification of the wave separation technique. It was shown that, under the conditions valid for the testing of low impedance cellular materials, the wave

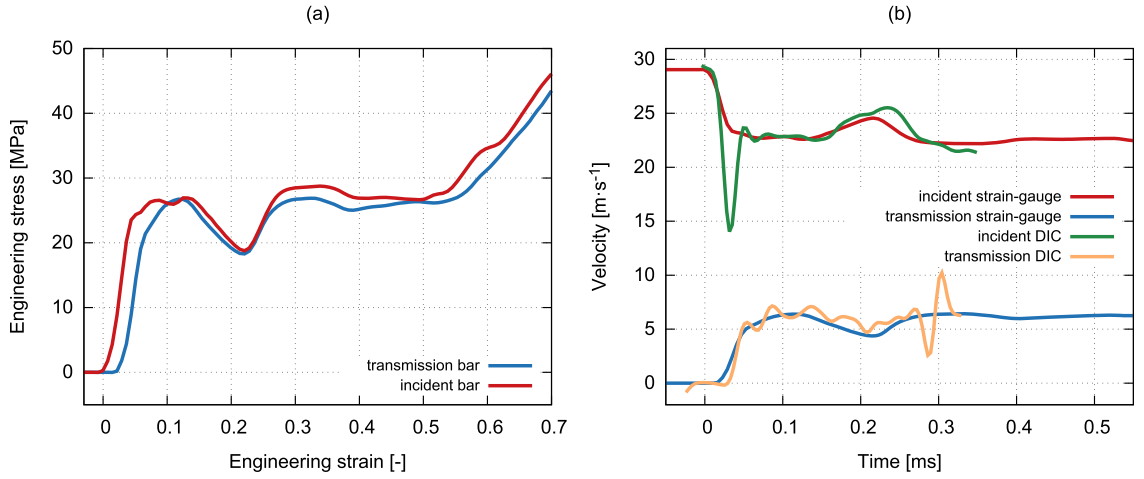

Fig. 19. The hybrid auxetic construct with a coating thickness of 120μm and rectangular struts tested at a maximum impact velocity of approximately 30$m{\cdot}s^{-1}$: Stress-strain diagram (a). Velocities evaluated from the strain-gauge signals compared with the DIC (b). Because of the high impact velocity, the DIC data are available only in a relatively narrow time window before the specimen moved from the area inspected by the camera.

separation technique can provide reliable decomposition of the strain pulses during the whole impact. The comparison of the velocities indicated by the DIC and strain-gauges is considered beneficial (in comparison to the displacements) as various errors can be better distinguished using the velocity measurements based on the DIC. Therefore, if successful, a more precise comparison of the measured quantities is possible.

- The DIC optimized for the sub-pixel tracking of the random speckle patterns mounted at the faces of the bars can be possibly employed as a sole technique for lower precision measurements of the velocity of the incident bar. With the known material properties of the incident bar, it would be possible to reconstruct the force present at the impact face using the wave separation approach inverse to the technique shown in the paper. The bar would have to be relatively long not to produce high frequency oscillations as, in such case, the wave reflections would be hidden in the noise and the velocity signal could not be used for the inverse separation method to calculate the actual force. The double differentiation of the DIC displacements cannot be used for the calculation of the actual acceleration (and force) as the differentiated signals are unsuitable due to significant noise. The DIC limits are particularly seen in the higher noise of the velocity signals, the high-speed camera imaging frequency and lower resolutions of the high-speed images. Nevertheless, the physical limit of the DIC for the evaluation of the velocity profiles with the employed state-of-the-art high-speed cameras lies significantly higher and was not reached in the presented method.
- The measurements with the visco-elastic bars can be significantly simplified in the OHPB under certain strict conditions. As the travel distance of the wave is short in the OHPB, the linear elastic model can be adopted instead of the frequency domain time-shifting to reconstruct the strain waves at the faces of the bars. Still, some technique that can reliably determine the dynamic material properties of the visco-elastic bars (e.g., [46]) has to be used to acquire the relevant parameters required for the linear elastic model. However, the straight-forward wave separation technique shown in the paper cannot be used for the visco-elastic bars as the distance travelled by the wave reflected from the free-end of the bar is too long and the reflected wave arrives severely attenuated and distorted.
- Both the aluminum alloy and PMMA bars were able to reliably record fine details of the crushing behavior of the cellular solids. The signals from the incident and transmission bar have comparable amplitudes and travel distance from the specimen. Therefore, problems with achieving the dynamic equilibrium typical for the SHPB are significantly reduced in this method. This can be supported by conclusions presented in [67], where, for the OHPB, the condition of the dynamic equilibrium has been achieved in a shorter time than in the conventional SHPB. In some of the presented experiments, force oscillations with an amplitude as low as $50-100N$ were reliably measured with the PMMA bars with a diameter of 20 mm.
- The method was successfully employed for the testing of several types of cellular solids, metamaterials and lattices in a high strain-rate dynamic compression. It was demonstrated that the two-sided instrumentation is a very important feature allowing for the analysis of the phenomena specific to the collapse of the individual lattice layers and the wave propagation through the specimen.
- Both closed-cell and open-cell metal foams were successfully tested using the setup, while the results are in good agreement with other papers [68,70].
- Additively manufactured auxetic lattices were tested using this method. The application of the OHPB arrangement allowed for the precise two-sided analysis of the collapse of the individual cell layers. As compared with our previous study regarding the same type of lattice tested in SHPB, the OHPB was able to compress the specimens to significantly larger strains than the SHPB with a comparable overall length at a similar strain-rate. Here, the OHPB represents an important alternative to the SHPB for testing materials at lower strain-rates, where the SHPB would require very long striker and both bars.
- Hybrid auxetic lattices manufactured by nanocrystalline coating process of the polymeric constructs printed using a 3D printer were tested using the method. As demonstrated, it was possible to measure the uncoated polymeric constructs that underwent instant disintegration as well as the hollow strut lattices. The auxetic constructs with a coating thickness of 60 μm exhibited an unusual behavior when the incident signal was, after the settling period, in all cases lower than the transmission signal until the densification of the structure, where both signals converged. The possible causes of this phenomenon including defects in the specimens and poor or asymmetric transfer of the strain-wave from the specimen to the bar were proposed. Interestingly, this behavior was not observed in the case of the constructs with a coating thickness of 120 μm. Here, the equilibrium of the dynamic forces was achieved quickly. The DIC indicated the same trend as the strain-gauges. Furthermore, the specimens of the different materials with even lower forces at the plateau region were measured with the same setup with a symmetrical response. Thus, it is considered that the phenomenon has to be caused by the specimen or the wave transfer at the interface between the specimen and the bar. Nevertheless, the material represents a light-weight and cost-effective alternative to the still expensive additively manufactured auxetic metamaterials. It was revealed that its auxetic behavior is much more profound than in the case of the previously tested structures [11] and has the potential for further development.
- The OHPB method in the presented form has a broad potential for further improvements and development. The method is particularly beneficial for a low to medium velocity impact and penetration testing (see Video S13) of large specimens and/or specimens that are difficult to produce in large numbers, where the analysis of the wave propagation effects is important and the specimen cannot be easily launched against a well-instrumented transmission bar or anvil. The presented arrangement also allows for designs with large diameter tubular bars or with large diameter inserts.

5. Conclusions

The DIHB method with the two-sided instrumentation using conventional strain-gauges was developed and tested with different types of cellular solids, metamaterials and auxetic lattice constructs subjected to uni-axial high strain-rate compression. The method is based on the previously proposed design of the OHPB, while it significantly increases its application envelope in terms of the impact velocity as well as the experiment duration. The wave separation technique based on boundary condition at the free-end of the bar was employed to reconstruct the velocity and force histories at the faces of the specimen. DIC was used as a tool for the measurement of the particle velocities at the bars in the vicinity of the specimen. It was shown that the comparison of the velocity indicated by the DIC with the strain-gauge signals can be used for the verification of the wave separation technique. This approach is considered superior to the possible comparison of the indicated displacements as the DIC velocity is more useful to analyze sources of errors and can reveal eventual problems with the experimental setup. The method was tested at impact velocities of up to 30 $\mathrm{m{\cdot}s^{-1}}$ with both linear elastic aluminum alloy bars and visco-elastic PMMA bars. The maximum velocity was constrained by the performance of the used gas-gun. It is believed that the maximum impact velocity can be further increased as no significant problems with the strain-gauges, wiring, linear guidance system or geometrical alignment of the bars during the impact at the maximum impact velocity were observed. Under certain circumstances, a simple approach using a linear elastic model can be employed for the evaluation of the experiments measured with the visco-elastic bars in the OHPB. The performance of the setup was evaluated in a series of experiments with different types of closed- and open-cell aluminum foams,

additively manufactured auxetic lattices, and hybrid nickel coated auxetic constructs subjected to dynamic uni-axial compression. The comprehensive direct impact testing methodology utilizing OHPB with two-sided instrumentation based on conventional strain-gauges and DIC was successfully employed for the high strain-rate loading of the cellular solids. The method represents an interesting, advanced, and straightforward alternative to the existing setups and is especially promising for the instrumented dynamic impact/penetration testing of large and/or expensive specimens, sandwiches or structural panels at low to medium impact velocities.

CRediT authorship contribution statement

Tomáš Fíla: Conceptualization, Methodology, Supervision, Investigation, Writing - original draft, Writing - review & editing. **Petr Koudelka:** Writing - original draft, Writing - review & editing. **Jan Falta:** Investigation, Writing - review & editing. **Petr Zlámal:** Investigation, Writing - original draft. **Václav Rada:** Investigation, Software. **Marcel Adorna:** Investigation, Data curation, Validation. **Stefan Bronder:** Resources. **Ondřej Jiroušek:** Supervision, Project administration, Funding acquisition.

Declaration of Competing Interest

The authors declare that they do not have any financial or nonfinancial conflict of interests

Acknowledgement

The authors acknowledge the financial support from the Operational Programme Research, Development and Education in the project INAFYM (CZ.02.1.01/0.0/0.0/16_019/0000766) and the Czech Science Foundation (project no. 19-23675S).

Supplementary material

Supplementary material associated with this article can be found, in the online version, at 10.1016/j.ijimpeng.2020.103767

References

[1] Xi H, Tang L, Luo S, Liu Y, Jiang Z, Liu Z. A numerical study of temperature effect on the penetration of aluminum foam sandwich panels under impact. Composites Part B: Engineering 2017;130:217–29. https://doi.org/10.1016/j.compositesb.2017.07.044.

[2] Jiroušek O, Doktor T, Kytýř D, Zlámal P, Fíla T, Koudelka P, et al. X-ray and finite element analysis of deformation response of closed-cell metal foam subjected to compressive loading. Jun of Inst 2013;8(02). https://doi.org/10.1088/1748-0221/8/02/c02012.C02012–C02012

[3] Vesenjak M, Veyhl C, Fiedler T. Analysis of anisotropy and strain rate sensitivity of open-cell metal foam. Mate Scien Engin: A 2012;541:105–9. https://doi.org/10.1016/j.msea.2012.02.010.

[4] Jung A, Diebels S. Synthesis and mechanical properties of novel ni/pu hybrid foams: a new economic composite material for energy absorbers. Adv Eng Mater 2016;18(4):532–41. https://doi.org/10.1002/adem.201500405.

[5] Tancogne-Dejean T, Spierings AB, Mohr D. Additively-manufactured metallic micro-lattice materials for high specific energy absorption under static and dynamic loading. Acta Mater 2016;116:14–28. https://doi.org/10.1016/j.actamat.2016.05.054.

[6] Novak N, Krstulović-Opara L, Ren Z, Vesenjak M. Mechanical properties of hybrid metamaterial with auxetic chiral cellular structure and silicon filler. Compos Struct 2020;234:111718. https://doi.org/10.1016/j.compstruct.2019.111718.

[7] Li T, Chen Y, Hu X, Li Y, Wang L. Exploiting negative poisson's ratio to design 3D-printed composites with enhanced mechanical properties. Mater Des 2018;142:247–58. https://doi.org/10.1016/j.matdes.2018.01.034.

[8] Hou S, Li T, Jia Z, Wang L. Mechanical properties of sandwich composites with 3D-printed auxetic and non-auxetic lattice cores under low velocity impact. Materials & Design 2018;160:1305–21. https://doi.org/10.1016/j.matdes.2018.11.002.

[9] Novak N, Starčevič L, Vesenjak M, Ren Z. Blast response study of the sandwich composite panels with 3D chiral auxetic core. Compos Struct 2019;210:167–78. https://doi.org/10.1016/j.compstruct.2018.11.050.

[10] Koudelka P, Jiroušek O, Fíla T, Doktor T. Compressive properties of auxetic structures produced with direct 3D printing. Materiali in Tehnologije 2016;50(3):311–7. https://doi.org/10.17222/mit.2014.204.

[11] Fíla T, Zlámal P, Jiroušek O, Falta J, Koudelka P, Kytýř D, et al. Impact testing of polymer-filled auxetics using split Hopkinson pressure bar. Adv Eng Mater 2017;19(10). https://doi.org/10.1002/adem.201700076.

[12] Fíla T, Koudelka P, Zlámal P, Falta J, Adorna M, Neuhäuserová M, et al. Strain dependency of poisson's ratio of SLS printed auxetic lattices subjected to quasi-static and dynamic compressive loading. Adv Eng Mater 2019;21(8). https://doi.org/10.1002/adem.201900204.

[13] Santosa SP, Arifurrahman F, Hafidz Izzudin M, Widagdo D, Gunawan L. Response analysis of blast impact loading of metal-foam sandwich panels. Procedia Eng 2017;173:495–502. https://doi.org/10.1016/j.proeng.2016.12.073.

[14] Kolsky H. An investigation of the mechanical properties of materials at very high rates of loading. Proceedings of the Physical Society Section B 1949;62(11):676–700. https://doi.org/10.1088/0370-1301/62/11/302.

[15] Peroni M, Solomos G, Pizzinato V. Impact behaviour testing of aluminium foam. Int J Impact Eng 2013;53:74–83. https://doi.org/10.1016/j.ijimpeng.2012.07.002.

[16] Peroni M, Solomos G, Babcsan N. Development of a Hopkinson bar apparatus for testing soft materials: application to a closed-cell aluminum foam. Materials (Basel) 2016;9(1):27. https://doi.org/10.3390/ma9010027.

[17] Deshpande V, Fleck N. High strain rate compressive behaviour of aluminium alloy foams. Int J Impact Eng 2000;24(3):277–98. https://doi.org/10.1016/S0734-743X(99)00153-0.

[18] Han F, Cheng H, Li Z, Wang Q. The strain rate effect of an open cell aluminum foam. Metall Mater Trans A 2005;36(3):645–50. https://doi.org/10.1007/s11661-005-0180-6.

[19] Wang P, Xu S, Li Z, Yang J, Zhang C, Zheng H, et al. Experimental investigation on the strain-rate effect and inertia effect of closed-cell aluminum foam subjected to dynamic loading. Materials Science and Engineering: A 2015;620:253–61. https://doi.org/10.1016/j.msea.2014.10.026.

[20] Yang B, Tang L, Liu Y, Liu Z, Jiang Z, Fang D. Localized deformation in aluminium foam during middle speed Hopkinson bar impact tests. Materials Science and Engineering: A 2013;560:734–43. https://doi.org/10.1016/j.msea.2012.10.027.

[21] Islam M, Brown A, Hazell P, Kader M, Escobedo J, Saadatfar M, et al. Mechanical response and dynamic deformation mechanisms of closed-cell aluminium alloy foams under dynamic loading. Int J Impact Eng 2018;114:111–22. https://doi.org/10.1016/j.ijimpeng.2017.12.012.

[22] Neuhäuserová M, Koudelka P, Falta J, Adorna M, Fíla T, Zlámal P. Strain-rate and printing direction dependency of compressive behaviour of 3D printed stainless steel 316l. Acta Polytechnica CTU Proceedings 2019:68–72. https://doi.org/10.14311/APP.2019.25.0068.

[23] Nishi M, Tanaka S, Vesenjak M, Ren Z, Hokamoto K. Experimental and computational analysis of the uni-directional porous (unipore) copper mechanical response at high-velocity impact. Int J Impact Eng 2020;136:103409. https://doi.org/10.1016/j.ijimpeng.2019.103409.

[24] Novak N, Vesenjak M, Tanaka S, Hokamoto K, Ren Z. Compressive behaviour of chiral auxetic cellular structures at different strain rates. Int J Impact Eng 2020;141:103566. https://doi.org/10.1016/j.ijimpeng.2020.103566.

[25] Wang L, Ding Y, Yang L. Experimental investigation on dynamic constitutive behavior of aluminum foams by new inverse methods from wave propagation measurements. Int J Impact Eng 2013;62:48–59. https://doi.org/10.1016/j.ijimpeng.2013.06.002.

[26] Adorna M, Zlámal P, Fíla T, Falta J, Felten M, Fries M, et al. Testing of hybrid nickel-polyurethane foams at high strain-rates using hopkinson bar and digital image correlation. Acta Polytechnica CTU Proceedings 2018:72–6. https://doi.org/10.14311/APP.2018.18.0072.

[27] Adorna M, Bronder S, Falta J, Zlámal P, Fíla T. Evaluation of hopkinson bar experiments using multiple digital image correlation software tools. Acta Polytechnica CTU Proceedings 2019:1–5. https://doi.org/10.14311/APP.2019.25.0001.

[28] Fíla T, Zlámal P, Falta J, Doktor T, Koudelka P, Kytýř D, et al. Testing of auxetic materials using hopkinson bar and digital image correlation. EPJ Web of Conferences. 183. EDP Sciences; 2018. https://doi.org/10.1051/epjconf/201818302045.

[29] Castro G, Nutt S, Wenchen X. Compression and low-velocity impact behavior of aluminum syntactic foam. Materials Science and Engineering: A 2013;578:222–9. https://doi.org/10.1016/j.msea.2013.04.081.

[30] Sudheer Kumar P, Ramachandra S, Ramamurty U. Effect of displacement-rate on the indentation behavior of an aluminum foam. Materials Science and Engineering: A 2003;347(1):330–7. https://doi.org/10.1016/S0921-5093(02)00608-1.

[31] Liang X, Luo H, Mu Y, Wu L, Lin H. Experimental study on stress attenuation in aluminum foam core sandwich panels in high-velocity impact. Mater Lett 2017;203:100–2. https://doi.org/10.1016/j.matlet.2017.05.036.

[32] Guo K, Zhu L, Li Y, Yu T, Shenoi A, Zhou Q. Experimental investigation on the dynamic behaviour of aluminum foam sandwich plate under repeated impacts. Compos Struct 2018;200:298–305. https://doi.org/10.1016/j.compstruct.2018.05.148.

[33] Lu G, Shen J, Hou W, Ruan D, Ong L. Dynamic indentation and penetration of aluminium foams. Int J Mech Sci 2008;50(5):932–43. https://doi.org/10.1016/j.ijmecsci.2007.09.006.

[34] Mohan K, Yip TH, Idapalapati S, Chen Z. Impact response of aluminum foam core sandwich structures. Materials Science and Engineering: A 2011;529:94–101. https://doi.org/10.1016/j.msea.2011.08.066.

[35] Gibson L, Ashby MF. Cellular solids: structure and properties. Cambridge University Press; 1999.Cambridge Solid State Science Series

[36] Ninan L, Tsai J, Sun C. Use of split Hopkinson pressure bar for testing off-axis composites. Int J Impact Eng 2001;25(3):291–313. https://doi.org/10.1016/S0734-743X(00)00039-7.
[37] Song B, Chen W. Loading and unloading split Hopkinson pressure bar pulse-shaping techniques for dynamic hysteretic loops. Exp Mech 2004;44(6):622–7. https://doi.org/10.1177/0014485104048911.
[38] Song B, Chen W. One-dimensional dynamic compressive behavior of epdm rubber. Journal of Engineering Materials and Technology, Transactions of the ASME 2003;125(3):294–301. https://doi.org/10.1115/1.1584492.
[39] Vecchio KS, Jiang F. Improved pulse shaping to achieve constant strain rate and stress equilibrium in split-hopkinson pressure bar testing. Metall Mater Trans A 2007;38 A(11):2655–65. https://doi.org/10.1007/s11661-007-9204-8.
[40] Song B, Chen W. Dynamic stress equilibration in split Hopkinson pressure bar tests on soft materials. Exp Mech 2004;44(3):300–12. https://doi.org/10.1177/0014485104041543.
[41] Jiang T, Xue P, Butt H. Pulse shaper design for dynamic testing of viscoelastic materials using polymeric SHPB. Int J Impact Eng 2015;79:45–52. https://doi.org/10.1016/j.ijimpeng.2014.08.016.
[42] Chen W, Lu F, Zhou B. A quartz-crystal-embedded split Hopkinson pressure bar for soft materials. Exp Mech 2000;40(1):1–6. https://doi.org/10.1007/BF02327540.
[43] Wang L, Labibes K, Azari Z, Pluvinage G. Generalization of split hopkinson bar technique to use viscoelastic bars. Int J Impact Eng 1994;15(5):669–86. https://doi.org/10.1016/0734-743X(94)90166-I.
[44] Zhao H, Gary G, Klepaczko JR. On the use of a viscoelastic split hopkinson pressure bar. Int J Impact Eng 1997;19(4):319–30. https://doi.org/10.1016/S0734-743X(96)00038-3.
[45] Mahfuz H, Al Mamun W, Haque A, Turner S, Mohamed H, Jeelani S. An innovative technique for measuring the high strain rate response of sandwich composites. Compos Struct 2000;50(3):279–85. https://doi.org/10.1016/S0263-8223(00)00118-5.
[46] Bacon C. An experimental method for considering dispersion and attenuation in a viscoelastic Hopkinson bar. Exp Mech 1998;38(4):242–9. https://doi.org/10.1007/BF02410385.
[47] Bacon C. Separation of waves propagating in an elastic or viscoelastic hopkinson pressure bar with three-dimensional effects. Int J Impact Eng 1999;22(1):55–69. https://doi.org/10.1016/S0734-743X(98)00048-7.
[48] Liu Q, Subhash G. Characterization of viscoelastic properties of polymer bar using iterative deconvolution in the time domain. Mech Mater 2006;38(12):1105–17. https://doi.org/10.1016/j.mechmat.2006.01.001.
[49] Bussac M, Collet P, Gary G, Othman R. An optimisation method for separating and rebuilding one-dimensional dispersive waves from multi-point measurements. application to elastic or viscoelastic bars. J Mech Phys Solids 2002;50(2):321–49. https://doi.org/10.1016/S0022-5096(01)00057-6.
[50] Park SW, Zhou M. Separation of elastic waves in split hopkinson bars using one-point strain measurements. Exp Mech 1999;39(4):287–94. https://doi.org/10.1007/BF02329807.
[51] Zhao H, Gary G. A new method for the separation of waves. application to the shpb technique for an unlimited duration of measurement. J Mech Phys Solids 1997;45(7):1185–202. https://doi.org/10.1016/S0022-5096(96)00117-2.
[52] Campana F, Mancini E, Pilone D, Sasso M. Strain rate and density-dependent strength of alsi7 alloy foams. Mater Scien Engin: A 2016;651:657–67. https://doi.org/10.1016/j.msea.2015.11.007.
[53] Reid S, Peng C. Dynamic uniaxial crushing of wood. Int J Impact Eng 1997;19(5):531–70. https://doi.org/10.1016/S0734-743X(97)00016-X.
[54] Radford D, Deshpande V, Fleck N. The use of metal foam projectiles to simulate shock loading on a structure. Int J Impact Eng 2005;31(9):1152–71. https://doi.org/10.1016/j.ijimpeng.2004.07.012.
[55] Zhao H, Elnasri I, Abdennadher S. An experimental study on the behaviour under impact loading of metallic cellular materials. Int J Mech Sci 2005;47(4):757–74. https://doi.org/10.1016/j.ijmecsci.2004.12.012.
[56] Liu J, He S, Zhao H, Li G, Wang M. Experimental investigation on the dynamic behaviour of metal foam: from yield to densification. Int J Impact Eng 2018;114:69–77. https://doi.org/10.1016/j.ijimpeng.2017.12.016.
[57] Duan Y, Du B, Shi X, Hou B, Li Y. Quasi-static and dynamic compressive properties and deformation mechanisms of 3D printed polymeric cellular structures with kelvin cells. Int J Impact Eng 2019;132:103303. https://doi.org/10.1016/j.ijimpeng.2019.05.017.
[58] Harris JA, Winter RE, McShane GJ. Impact response of additively manufactured metallic hybrid lattice materials. Int J Impact Eng 2017;104:177–91. https://doi.org/10.1016/j.ijimpeng.2017.02.007.
[59] Lopatnikov SL, Gama BA, Jahirul Haque M, Krauthauser C, Gillespie JW, Guden M, et al. Dynamics of metal foam deformation during Taylor cylinder-Hopkinson bar impact experiment. Compos Struct 2003;61(1):61–71. https://doi.org/10.1016/S0263-8223(03)00039-4.
[60] Taylor IG. The use of flat-ended projectiles for determining dynamic yield stress i. theoretical considerations. Proc R Soc London, Ser A 1948;194:289–99. https://doi.org/10.1098/rspa.1948.0081.
[61] Whiffin AC, Taylor IG. The use of flat-ended projectiles for determining dynamic yield stress ii. tests on various metallic materials. Proc R Soc London, Ser A 1948;194:300–22. https://doi.org/10.1016/0003-4916(63)90068-X.
[62] Hiermaier S, Meenken T. Characterization of low-impedance materials at elevated strain rates. J Strain Anal Eng Des 2010;45(6):401–9. https://doi.org/10.1243/03093247JSA584.
[63] Lea LJ, Jardine AP. Two-wave photon doppler velocimetry measurements in direct impact Hopkinson pressure bar experiments94; 2015. https://doi.org/10.1051/epjconf/20159401063.
[64] Casem D, Zellner M. Kolsky bar wave separation using a photon doppler velocimeter. Exp Mech 2013;53(8):1467–73. https://doi.org/10.1007/s11340-013-9735-4.
[65] Cowie T, Gurnham CWA, Braithwaite CH, Lea L. Impact performance of aluminium foams in a direct impact hopkinson bar. AIP Conf Proc 2018;1979(1):110003. https://doi.org/10.1063/1.5044922.
[66] Pang X, Du H. Investigation on dynamic penetration of closed-cell aluminium foam using in situ deceleration measurement. Composites Part B: Engineering 2016;100:78–90. https://doi.org/10.1016/j.compositesb.2016.06.040.
[67] Govender RA, Curry RJ. The "open" hopkinson pressure bar: towards addressing force equilibrium in specimens with non-uniform deformation. Jun Dyna Behav of Mater 2016;2(1):43–9. https://doi.org/10.1007/s40870-015-0042-2.
[68] Dannemann KA, Lankford Jr. J. High strain rate compression of closed-cell aluminum foams. Mater Sci Eng, A 2000;293(1):157–64. https://doi.org/10.1016/S0921-5093(00)01219-3.
[69] Elnasri I, Pattofatto S, Zhao H, Tsitsiris H, Hild F, Girard Y. Shock enhancement of cellular structures under impact loading: part i experiments. J Mech Phys Solids 2007;55(12):2652–71. https://doi.org/10.1016/j.jmps.2007.04.005.
[70] Shen J, Lu G, Ruan D. Compressive behaviour of closed-cell aluminium foams at high strain rates. Composites Part B: Engineering 2010;41(8):678–85. https://doi.org/10.1016/j.compositesb.2010.07.005.
[71] Xu S, Ruan D, Beynon J, Lu G. Experimental investigation of the dynamic behavior of aluminum foams. Materials Science Forum 2010;654–656:950–3.DOI:10.4028/www.scientific.net/MSF.654-656.950